Southern Ocean precipitation observed from satellite and ground instrumentation at Macquarie Island

Emily Tansey

A thesis

submitted in partial fulfillment of the

requirements for the degree of

Master of Science

University of Washington

2020

Committee:

Roger Marchand

Lynn McMurdie

Chris Bretherton

Program Authorized to Offer Degree:

Atmospheric Sciences

University of Washington

Abstract

Southern Ocean precipitation observed from satellite and ground instrumentation at Macquarie Island

Emily Tansey

Chair of the Supervisory Committee:

Professor Roger Marchand

Atmospheric Sciences

The seasonal and synoptic variability of Southern Ocean (SO) precipitation are studied using ground-based observations at Macquarie Island. Parsivel disdrometer and W-band radar measurements are blended to determine precipitation thermodynamic phase, hydrometeor size distributions and rain rates, enabling a more detailed examination of SO precipitation characteristics than has been previously possible. In particular, we find that small-particle precipitation occurs to 30 to 50% of the time, depending on the season. Glaciated precipitation is observed most often during fall and winter, and to the southeast of SO cyclonic systems. Comparisons of the Macquarie Island observations to precipitation estimates (retrievals) based on measurements from the CloudSat Cloud-Profiling Radar show good agreement in the distribution of rain rates for rates >0.5 mm/hour, which comprise the bulk of the total accumulated precipitation. However, CloudSat does miss much of the lighter precipitation that is comprised primarily of small particles (<0.5 mm) and occurs most frequently over the SO.

TABLE OF CONTENTS

Chapter 1 Introduction

The Southern Ocean (SO) makes up a large portion of the southern hemisphere, and is a region where climate models have been shown to have large biases in top-of-atmosphere radiative fluxes. In particular, climate model simulations commonly show an excess of absorbed shortwave radiation over the SO at mid to high latitudes (Trenbarth & Fasullo, 2010). Clouds, specifically a lack of sufficiently reflective low-altitude cloud, are the cause of most of this SO radiation bias in the models (Bodas-Salcedo et al. 2016). SO low clouds often contain multiple layers and supercool water that largely control their optical properties (Huang et al. 2016), and have proven difficult for models to simulate well (Kay et al. 2016). The excess in absorbed shortwave radiation has been shown to increase surface heating and alter both local and global ocean and atmosphere circulations. For example, Hwang and Frierson (2012) show that SO clouds bias global cross-equatorial energy transport, resulting in a biased southward shift in tropical precipitation patterns.

In addition to its importance in global energy and water cycles (Stephens, 2012), precipitation plays a key role in shaping low cloud occurrence and cloud microphysical properties, such as cloud particle size, which has a significant impact on the cloud reflectivity (and total absorbed shortwave radiation). Precipitation affects clouds directly through collisions between precipitation and cloud-sized particles (collision-coalescence processes: accretion, aggregation, riming) and various other small-scale microphysical processes (ice multiplication and secondary ice production), as well as indirectly through the impact that precipitation has on aerosols (scavenging) and the thermodynamical structure of the boundary layer through evaporative cooling (Albrecht, 1993). SO low clouds have been observed to precipitate frequently, with a mixture of ice and liquid precipitation (Chubb et al. 2013). It is not known how much precipitation falling from SO clouds is liquid or ice, and much of the ice precipitation originating from low clouds is thought to be a result of secondary ice processes (Mace and Protat 2017).

Precipitation measurements are particularly sparse over regions like the SO, where there is little land and few ground-based observation sites exist. This necessitates the use of satellite retrievals and assimilated data for climate model evaluation. Yet retrieval and assimilated precipitation fields are very uncertain at high latitudes. For instance, Behrangi et al. (2014, 2016) found that global precipitation sources commonly relied on for model parameterization (specifically the Global Precipitation Climatology Project (GPCP) and Climate Prediction Center Merged Analysis of Precipitation (CMAP) datasets) underestimate daily precipitation rates by 5.4% and 13.3%, respectively for the Southern Hemisphere (0-80^{o}S) as compared with a precipitation product he has developed that includes CloudSat retrievals. It is therefore crucial to ascertain where the mismatch across observational retrievals arises, and validate satellite products in particular.

Satellite observations have been heavily relied on to retrieve key properties such as the total amount of liquid water or ice embedded within clouds, cloud-particle size, as well as precipitation occurrence, rate, and phase (liquid, frozen, mixed). Yet much remains uncertain about the ability of satellites to accurately determine cloud and precipitation properties in this region (Wang et al. 2015; Huang et al. 2016). In particular, extensive light precipitation, frequent mixed phase conditions, and near-surface melting layers make retrieval of SO precipitation properties from satellite challenging (Haynes et al. 2009).

CloudSat's Cloud Profiling Radar (CPR) provides arguably the most accurate precipitation estimates over the SO. The CloudSat CPR is a 94-GHz nadir-looking radar, measuring power backscattered by hydrometeors (both clouds and precipitation) as a function of distance from the radar (Stephens, 2008). Nonetheless, significant differences between CloudSat's estimates of precipitation occurrence and rates versus those from passive-microwave measurements indicate that further validation over the SO is necessary (Behrangi et al. 2014; Huang et al. 2012).

The CloudSat CPR suffers significant limitations from ground clutter effects, that is, interference or false signals generated by the interaction of the radar pulse with the surface.

The ground clutter makes it difficult for these radars to make meaningful measurements of hydrometeors closer than about 750 m above the surface (Marchand, 2008). The ground clutter impacts both radar datasets, especially those regarding precipitation from low/shallow clouds.

Between March 2016 and March 2018, an array of ground instrumentation was deployed as part of the Macquarie Island Cloud and Radar Experiment (MICRE) as a basis for comparison with satellite observations. Located at 54.508S 158.948E, Macquarie Island is an ideal location for studying the SO atmosphere. The instrumentation deployed during MICRE included a particle size-velocity (Parsivel) disdrometer, microwave radiometer, lidar and (for the first year) cloud radar, also operating at 94 GHz. These measurements augmented ongoing surface meteorological and radiosonde observations that have been made from the island for many years (Adams, 2009).

This work blends timeseries from the Parsivel and radar together to form a detailed climatology of SO precipitation phase, rates and drop size distributions. Disdrometers are not particularly well-suited to detect light precipitation and are prone to a number of additional errors identified in Chapter 2, and so I blend the disdrometer measurements with the cloud radar retrievals because the radar is able to detect very light precipitation (with rate less than 0.01 mm/hr).

Unfortunately, the Parsivel vendor-supplied algorithms did not work well during MICRE and required substantial post-processing. An algorithm was written to improve upon the vendor's output of these characteristics (Appendix I).

In Chapter 3 results are presented on the MICRE precipitation data in different cyclone sectors. That is, I use the sector in which Macquarie Island lay with respect to the nearest storm (low-pressure) center to relate precipitation properties to the dynamics of the synoptic environment. This section also analyzes the overall characteristics of SO precipitation, the seasonal cycle, and other characteristics of precipitation in different storm sectors. In Chapter 4, I also compare the MICRE observations to CloudSat retrievals and discuss how

generalizable the observations at Macquarie Island are to the SO at large, with conclusions and next steps given in Chapter 5.

Chapter 2 Data and Methods

This chapter discusses instrumentation used during the MICRE project, observational data and several newly developed algorithms to retrieve precipitation information. A blending algorithm used to combine measurements from different instruments is described. Data used in the environmental and satellite comparisons are also detailed.

2.1 Meteorological data at Macquarie Island

The Australian Bureau of Meteorology operates a small research station on Macquarie Island, which is staffed year round. Meteorological variables including wind speed, wind direction, temperature, relative humidity and pressure at the surface are recorded. The site also collects tipping bucket precipitation data, for which the associated time series stretched back continuously until 1948 and has been featured in past studies to assess reanalysis and satellite retrievals (Wang et al. 2015). However, the bucket tips after every 0.2 mm of accumulation, making light precipitation occurrence difficult to recognize.

2.2 Parsivel disdrometer

Characteristics like average hydrometeor size, thermodynamic phase and precipitation rate are crucial to the SO climatology. This work relies heavily on physics extracted from particle size-velocity ("Parsivel") disdrometer measurements, as detailed in the next sections.

2.2.1 Instrument and vendor retrieval overview

The Parsivel disdrometer is a laser-based optical precipitation sensor developed by OTT Messtechnik. It consists of two hooded segments: one for the laser transmitter and one for the photodiode detection receiver. These are separated by a distance of 180 mm. Laser light is spread horizontally to form a beam 30 mm wide and 1 mm thick, creating a detection area of 180×30 mm^2 through which precipitating particles fall (Figure 2.1). The laser emits a wavelength of 695 nm (with nominally 3mW of power).

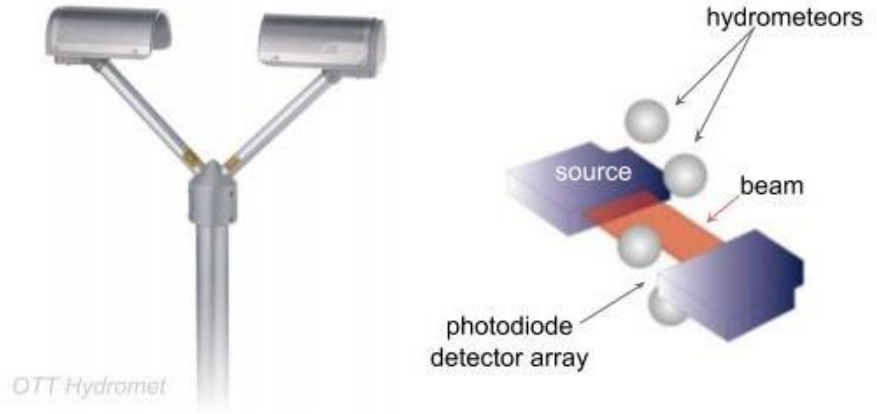

Figure 2-1 Parsivel disdrometer instrument schematic (Löffler-Mang & Joss, 2000)

Raw Parsivel output consists of a time-dependent voltage signal; as particles pass through the laser beam, this signal is dampened in proportion to their size. Particle equivalent diameter is therefore the first physical quantity estimated by the vendor's algorithm (Battaglia et al. 2010). Small liquid precipitating particles (diameter <1 mm) are spherical, but larger hydrometeors take on a multitude of shapes. Raindrops become oblate spheroids due to air drag, while frozen hydrometeors shapes are even less consistent because of their asymmetrical nature. The retrieval relies on the assumption that particles fall with their major axis horizontally oriented. The vendor's calculation of equivalent diameter in proportion to dampened voltage signal is therefore highly approximate.

Although the vendor's algorithms are proprietary, Battaglia et al provide insight into how the detected cross section is equated to particle size (Figure 2.2). From the equivalent diameter, a prescribed aspect ratio is assigned to estimate the vertical dimension. This is key for the fall speed approximation. The voltage dampening time's full width at half maximum dt is measured and used to estimate the particle fall velocity, v_{fall}. Equivalent diameter and fall speeds are output in 2D 32×32 bin histograms (unit: counts), generating level 2 data. An example is shown in Figure 2.3. The y-axis bins represent fall speed, the dependent variable (unit: m s^{-1}); diameter (unit: mm) occupies the x-axis. Different particles occupy different regions of this 2D space (to some degree) and enable some identification of the thermodynamic phase of the precipitation. Nominally, the instrument detects liquid particles

with diameters between 0.2 – 5 mm and solid particles between 0.2 – 25 mm, but bins below 1 mm, while having some counts, experience frequent undercounting.

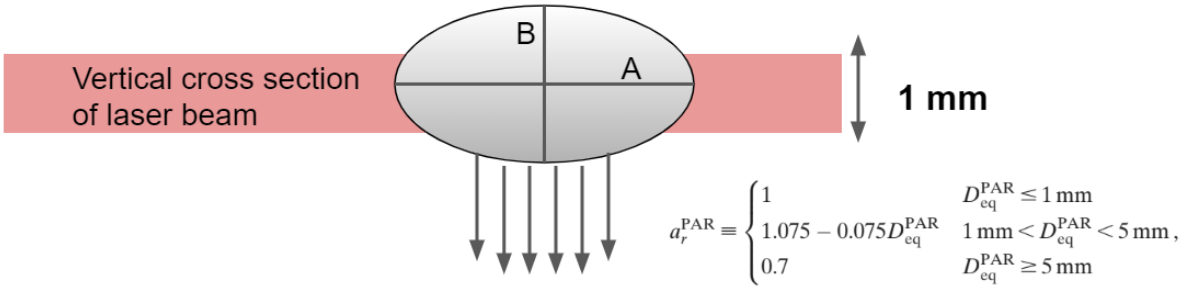

Figure 2-2 From the equivalent diameter D_{eq}^{PAR}, the aspect ratio a_r^{PAR} (A:B) is calculated and the vertical dimension approximated. Different D_{eq}^{PAR} determine which aspect ratio is assigned.

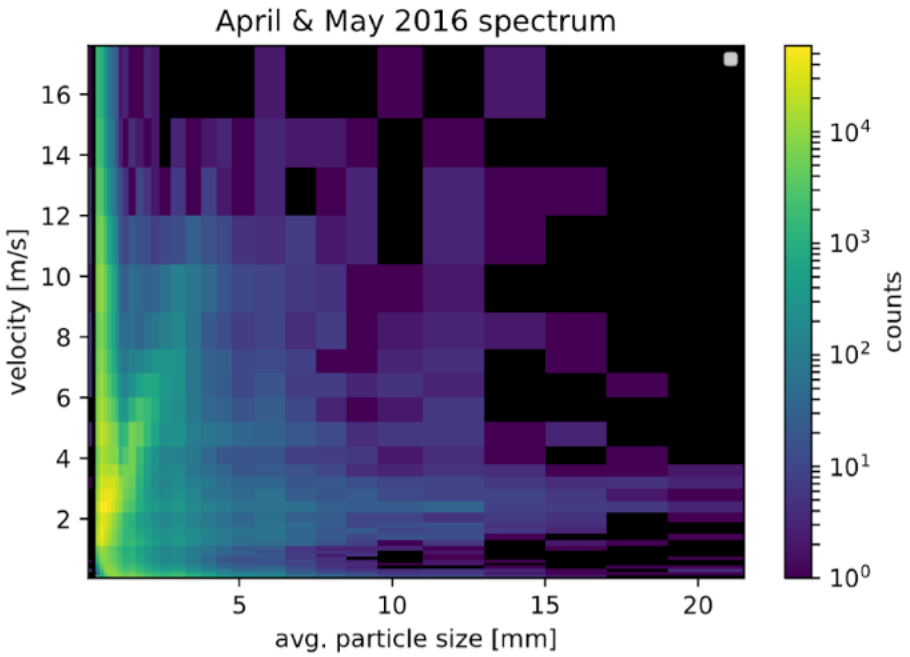

Figure 2-3 Example of particle size-velocity Parsivel histogram from the first two months of the MICRE project.

A number of studies have discussed considerations that go into determining phase (Battaglia et al. 2010; Löffler-Mang & Joss, 1999; Raupach & Berne, 2015). The main method in the vendor's "weather code" (precipitation type) designation is a bin's location on the histogram. For instance, equivalent diameters larger than 5 mm are assumed to be frozen; if they fall faster than some threshold velocity, they are classified as hail instead of snow.

2.2.2 Parsivel sensitivity limitations and error identification

Two major limitations of the Parsivel are *(i)* the instrument's lack of sensitivity to small-particle precipitation and *(ii)* its susceptibility to wind-induced biases (Friedrich et al.

2013). Large errors associated with wind biases, among other factors, prompted us to reprocess the raw (level 2) spectra via a new retrieval we call the **Parsivel Improved Rates and Types (PIRAT)** algorithm. PIRAT identifies precipitation phase, corrects for density in the event that precipitation is frozen, and then calculates DSDs, rates and accumulation.

Our motivations for developing a separate Parsivel retrieval are numerous: first, the vendor's algorithm is proprietary. Since little is known about the weather codes, it is difficult to determine how to use them. Secondly, the vendor's output consistently overlooks light precipitation (low rain rates) due to poor optical sensitivity. Thirdly, (semi-)frozen precipitation appears to lack any sort of density correction, resulting in too-high retrieved rates. Finally, an inconsistency in the MICRE data loggers resulted in the loss of all weather codes past the third month of the project. Even if the vendor's weather codes were reliable, most of the timeseries has none.

2.2.3 PIRAT algorithm

The operating principle behind PIRAT is to compare occupied bins in a size-velocity spectrum to fall speeds for various precipitation types, as plotted in Figure 2.4. The rain curve was taken from the well-known relation derived in Gunn and Kinzer's 1949 paper on rain terminal fall speed. Ice pellet and snow fall speed relations were derived by curve-fitting their respective composited spectra, as designated by the vendor's weather codes from the first three months of MICRE. Lastly, the wet snow or mixed phase equation was derived using bins between the rain and ice pellet spectral regions.

The algorithm has a tuneable timestep up to 1-minute resolution, is written in Python and is now available on GitHub at *https://github.com/etansey/PIRAT_algorithm*. Technical details of PIRAT's inner workings are in Appendix I. The following sections explain the sources of these errors and how they are addressed.

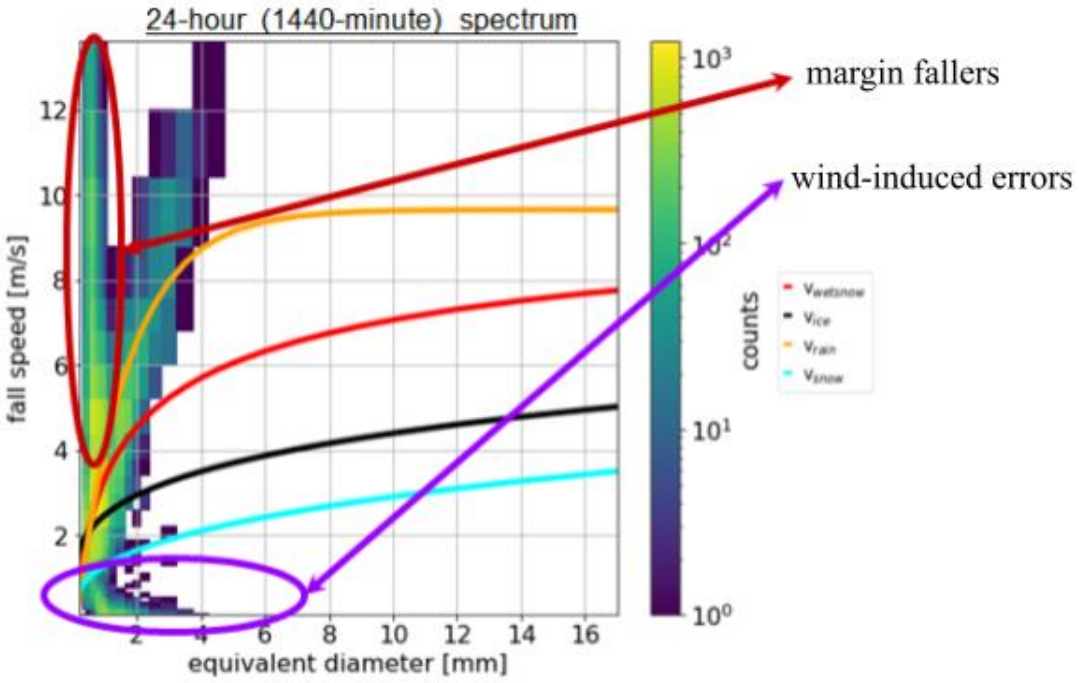

Figure 2-4 Warm rain spectrum exemplifying the two commonly observed types of noise. The overlaid curves are fall speeds as a function of diameter for rain (gold solid line), wet snow (red), ice pellets (black) and snow (cyan).

2.2.4 Undersampling of small-particle precipitation

The disdrometer lacks sensitivity to small-particle precipitation. In response to this issue, we reduced the 1-minute temporal sampling rate to 5 minutes to improve signal-to-noise.

Figure 2.4 points out the noisiest regions on an uncorrected size-velocity spectrum. During both light and heavier precipitation, “margin fallers” are expected to arise when particles pass partially through the beam at one of the edges, or can result when particles splash/break apart after colliding with the beam’s protective covering. These get recorded as unrealistically fast-falling small particles. Figure 2.4 shows the 24-hour spectrum for a day with featuring only warm rain at Macquarie. The margin fallers can be seen extending vertically on the left side.

2.2.4.1 Wind-induced errors

Regarding the second problem, preliminary MICRE data analysis shows a tendency towards diameter overestimation and fall speed underestimation under northerly and north-westerly winds. The laser beam ideally should be transverse to the wind. But, as is typical,

the instrument was on a fixed mount point with the laser aligned north-south (broadside to the prevailing westerly winds). The exact cause of the wind-contamination is unclear but splashing droplets off the instrument housing may be a factor; other factors such as turbulent air motions and reduction in the available-sampling volume may also be involved. Hydrometeor velocities in particular are falsely estimated. At times one sees pure rain fall speeds shifted downward, deviating from the expected fall speed curves and giving spectra a blurry look.

To address this issue, a correction factor as a function of wind speed and direction was sought. Warm rain cases (surface temperature > 5^{o}C) were used for this approach because of their straight forward meteorological identification and characteristic spectral shape. However, very low correlation between velocity errors and wind speed/direction was observed (Fig. 3, Appendix I). Rather, spectral blurring was observed at all wind speeds and directions, with no significant pattern. Therefore, as an alternative, an average velocity shift was calculated to put rain counts on the rain curve during windy conditions. This was done

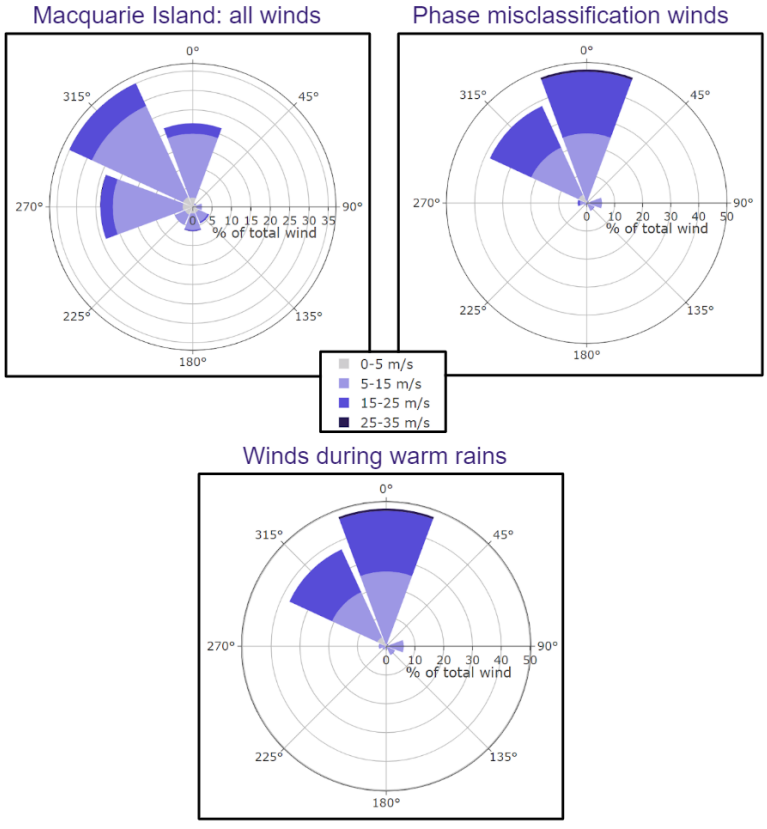

Figure 2-5Macquarie Island wind profiles corresponding to (i) all meteorological data, (ii) time periods where phase was liquid but misclassified as frozen and (iii) correctly classified warm rain time periods.

for each diameter class (Fig. 4, Appendix I) for data composited across all high-wind rain

events. PIRAT applies this constant shift as a function of diameter when a blurred spectrum is encountered.

2.3 W-band Doppler radar

In addition to the Parsivel, an upward-facing (vertically pointed) W-band Doppler radar was on site for the first year of MICRE. The W-band radar operates at a frequency of 94 GHz (3.2 mm wavelength) (Kollias, 2005). The radar supplements Parsivel measurements in the small-particle regime; as stated previously, the disdrometer often misses particles below about 0.5 to 1 mm in diameter. For particles at this order of magnitude, the radar's 3.2 mm wavelength enters the Rayleigh scattering regime. The expected type of scattering is determined by the size parameter x:

$$x = \frac{2\pi \cdot r}{\lambda} \quad (1)$$

Rayleigh scattering occurs for x less than about 0.1.

The majority of Macquarie Island precipitating particles have radii on the order of 0.5 mm or less, as demonstrated by the results of this work. A fuller picture is therefore provided by blending observations from both the radar and Parsivel. A Rayleigh scatterer's scattering cross-section σ_s relates to its radius via $\sigma_s \propto r^6 \cdot \lambda^{-4}$, and a small change in radii has a large impact on the radar reflectivity. The radar also measures the Doppler effect (change in frequency due to motion toward or from the radar) which also depends on the particles size, as was the case for the Parsivel. The radar retrieval follows Frisch et al. (1995) with Doppler velocity averaging following Orr and Kropfli (1999).

This retrievals relies on the assumption of Rayleigh scattering, and consequently is only reliable for light precipitation composed of small particles. Data quality flags are included in the data product and denote situations with *(i)* no lidar cloud base available, *(ii)* lidar cloud base below 250 m (the radar's minimum detectable ranges is about 125 m), *(iii)* extrapolation because dBZ was too small or large (outside the expected range for Rayleigh scattering) and *(iv)* estimated fall velocity less than 0.3 m s^{-1} or above 3 m s^{-1} (if e.g. velocity is not measured well or again particles are too large).

2.3.2 Melting layer identification

Generally, the altitude at which frozen precipitation starts melting can be located from observed vertical jumps in reflectivity. This sudden increase or decrease in reflectivity, called a bright band or dark band, occurs when the precipitation phase begins to transition from frozen to liquid. The melting layer is therefore often used to approximate the 0°C isotherm (Austin & Bemis, 1949).

A bright band results because the dielectric constant changes drastically during the phase transition from ice to liquid. The dielectric constant of ice is smaller than liquid water at microwave frequencies. Furthermore, snowflakes often melt on their outer shell initially, making a particle look like a very large rain drop. This difference is less pronounced at W-band than at lower frequencies, however, because the dielectric constants of ice and liquid are closer in value at 94-GHz than lower frequencies. Water-coated frozen particles in the melting layer are typically in the Mie regime and don't necessarily backscatter more energy than pure raindrops below the melting level. Without the convenience of a consistent bright band, we use an alternative melting layer algorithm based on the W-band Doppler velocity.

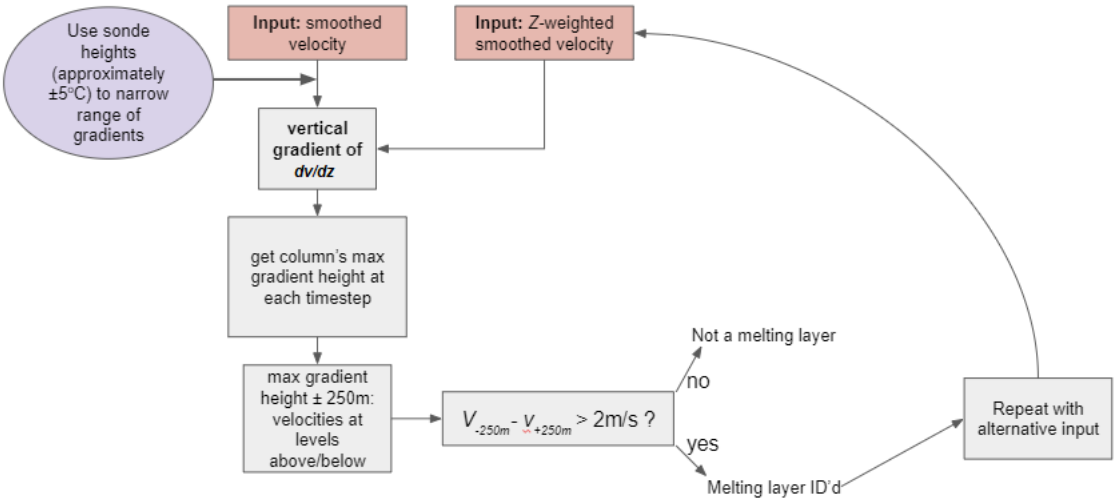

Figure 2-6 Melting layer identification scheme.

Figure 2.6 displays a schematic diagram of the steps that go into identifying a melting layer without relying on the bright band. The radar data we used has 25 m height resolution, spanning from about 125 m above the surface up to 1.2 km. The radar time resolution is 12 seconds. Additionally, twice-daily radiosondes at 00:00 and 12:00 are launched at Macquarie

from 8 m above sea level. Because of their different time resolution and expected westerly advection, the radiosondes are used as solely guidelines to approximate the height -5^{o} to 5^{o}C range.

First, a running mean of 2 minutes is taken for both the velocity and reflectivity. This is done to smooth the signal and decrease the impact of noise. Two separate vertical profiles are created: *(i)* a smoothed velocity profile (simply an averaged velocity) and *(ii)* a reflectivity-weighted velocity profile (referred to as v_z). Reflectivity weighting ensures that high velocities resulting e.g. from strong winds or downdrafts do not confuse the algorithm where no precipitation is present. v_z is defined by

$$v_Z = \frac{\sum_{i,j} Z \cdot v}{\sum_{i,j} Z} \tag{7}$$

where $Z = 10^{dBZeq}/10$ is the equivalent reflectivity factor and dBZ_{eq} is the returned signal, in decibels relative to height Z.

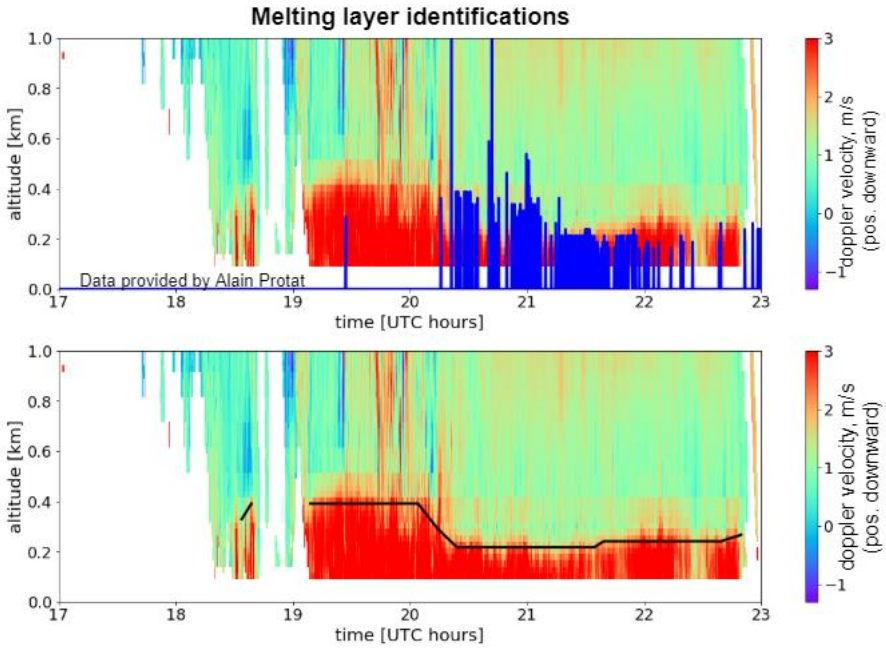

Figure 2-7

Next the gradient of the profiles (dv_z/dz, with weighted velocity v_z and vertical coordinate z) is calculated. The gradient is taken within a height range corresponding to around ±5^{o}C from a nearby-in-time radiosonde if available; otherwise a climatological range is used.

Velocities at ±250 meters above the dv_z/dz maximum are compared. If the fall speed has increased by 2 m s^{-1} or more, this defines melting layer height at each time step. Otherwise, the time step is not considered to have a melting layer. An example of the output is shown in Fig 2.7, where the top plot uses a simple velocity gradient around ±5°C with no smoothing (blue lines). The benefit to averaging and Z-weighting can be seen in the bottom plot's smoothness in time (black line), yielding a more realistic melting layer representation.

2.4 Synoptic environment data

The synoptic environment is characterized by the distance to the nearest extratropical cyclone (low pressure) center, as well as the quadrant in which the MICRE site resides relative to the low pressure center. Data is taken from the NASA Modeling, Analysis and Prediction Climatology of Midlatitude Storminess (MCMS). Storm center locations are detected using sea-level pressure minima from ERA-Interim 1.5° horizontal resolution data. The lows are tracked over time, and the corresponding closed pressure contour surrounding the center is used to estimate the domain of spatial influence (Bauer et al. 2016).

Corresponding cold fronts are detected using a mix of two methods: *(i)* dry temperature gradient at 1 km above the surface (Hewson, 1998) and *(ii)* change in 850 hPa winds (Simmonds et al. 2011). Warm front detection relies exclusively on the 1 km above-surface criteria. In occluded systems, the distinction between cool and warm air masses are not well-identified, often resulting in unreliable frontal positions.

The data set used here was put together for the MICRE project by Saisai Ding of Peking University, and contains cyclone center and front locations nearest to Macquarie Island at a time resolution of 6 hours. The nearest point to Macquarie is deduced using MCMS interpolated frontal lines. The quadrant Macquarie falls in relative to the storm center is calculated for each front within a 30° × 30° grid cell. Each quadrant is a 15°×15° square centered on the storm center, as shown in Fig. 2.8. In section 3, precipitation characteristics are explored based on which quadrant the island falls in. If Macquarie does not fall within 30°×30° of a center, the storm is put in a separate category, “far”.

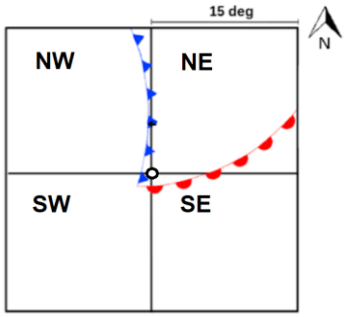

Figure 2-8 Geographic orientation of quadrants with respect to the storm center.

2.5 CloudSat CPR products

CloudSat was launched as part of the A-Train satellite constellation on 28 April 2006, into a sun-synchronous polar orbit. The minimum mission lifetime was intended to be 2 years, yet several output epochs and nearly 14 years later, the satellite continues to provide useful observations to the remote sensing community, especially of high latitudes (Mitrescu et al, 2009). Measured by CloudSat's Cloud Profiling Radar (CPR), this comparison study relies on 2C-PRECIP-COLUMN data from the most recent iteration of the product (R05, released in 2019).

The CPR is a 94-GHz nadir-pointing radar with 240 m vertical sampling and 500 m resolution. Data is averaged over about a 0.16 second interval, yielding a footprint of about 1.4×2.5 km^2 with 1.1 km along-track sampling distance. Because it is a nadir-pointing radar, the CPR collects observations in a 2D “curtain”. Multiple photon scattering frequently occurs in the data, causing hydrometeor-free regions below cloud have a measureable return signal from the multiple scattering, which must be accounted for in the retrieval process.

2.5.1 Retrieving precipitation characteristics over ocean

CPR retrievals rely heavily on the path-integrated attenuation (PIA) of the radar signal as it returns to the detector. The PIA is determined from the difference in the measured surface backscatter from what is expected under clear-sky conditions, and includes correcting for water vapor absorption effects (usually based on ECMWF analysis). Composited clear-sky backscatter profiles for a multitude of different surface types (urban, cropland, evergreen, tundra, water, etc.) have been extracted from the data (Mitrescu et al. 2009), with values for the ocean depending on sea-surface temperature and wind-induced roughness. Typically,

windspeed measurements from e.g. the microwave radiometer on board Aqua, paired with SST from ECMWF, are used to estimate the expected ocean clear-sky backscatter (Haynes et al. 2009). The measured PIA is combined with the observed radar reflectivity profile, and a model for the vertical distribution of condensate (including a melting layer, as needed) is used to derive the precipitation rate. The formulation is complex, and details are given in Mitrescu et al (2009).

Chapter 3 Results

3.1 Blended disdrometer and radar precipitation dataset

The blended dataset is a timeseries merge of the PIRAT-processed disdrometer and W-band radar for the first year of the MICRE project (April 2016-March 2017). This section looks at frequency of precipitation broken down by phase, where possible, and the seasonal cycle of its characteristics.

3.1.1 Seasonal frequency of precipitation phases

Figure 3.1 shows the percent of the time that precipitation is detected, with the following frequencies of occurrence: fall (MAM) 53.8%, winter (JJA) 60.5%, spring (SON) 47.9% and summer (DJF) 37.1%. When precipitating, small- and large-particle precipitation are plotted as distinct categories. A further breakdown of large-particle precipitation into thermodynamic phases (rain, ice pellets, wet snow and snow) is shown in Figure 3.2. It is clear from Figure 3.2 that, although frozen precipitation occurs most in winter, it observed in every season.

Precipitation occurs more often over Macquarie Island than reported by Wang et al. (2015). Wang et al. report “no detectable” precipitation 63.6% of the time using a three-hour tipping bucket accumulation to calculate rate of precipitation. The higher sensitivity of the MICRE instrumentation enables identification of lighter and small-particle precipitation not detected by a tipping bucket. The majority of small-particle precipitation is expected to be liquid drizzle. Using a combination of W-band radar and micropulse lidar, Protat and Mace (2018) found that 14% of all summer (DJF) clouds had frozen precipitation directly below cloud base. This percentage does not, however, indicate how much of the precipitation is still frozen upon reaching the surface.

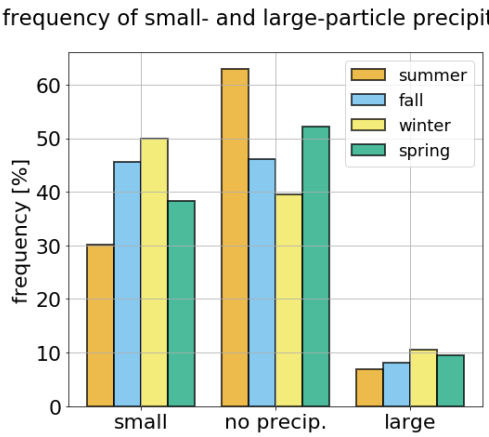

Figure 3-1 Frequency of occurrence (percent of the time) of small-particle, large-particle and no detectable precipitation.

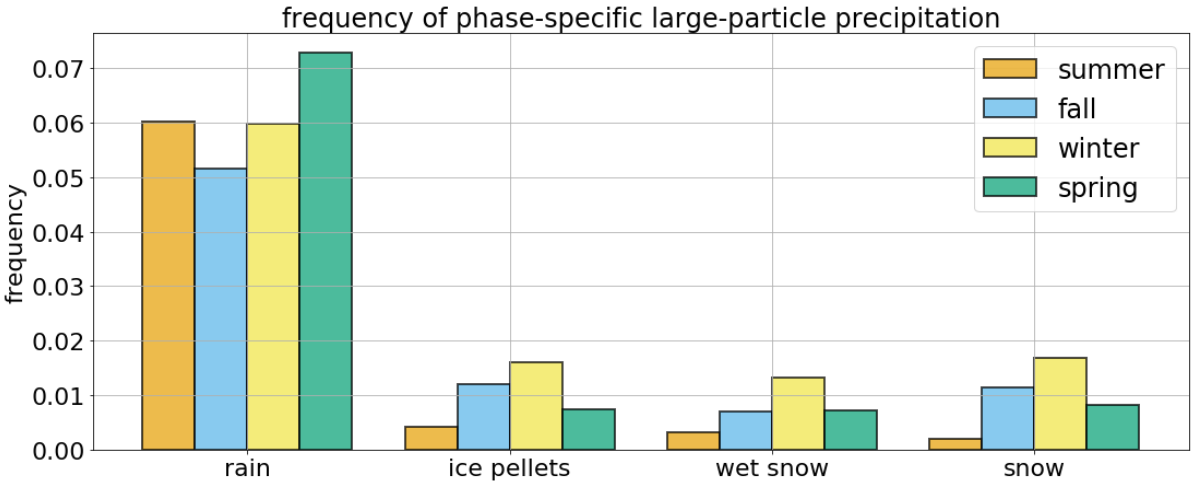

Figure 3-2 Frequency distribution of PIRAT-designated large-particle phases.

3.1.2 Blended seasonal particle size distributions

Fig. 3.3 shows two seasonally-separated PIRAT particle size distributions for all precipitation (top) and rain only (bottom); all PIRAT-designated precipitation types are included in the top plot, whereas only events identified as rain are plotted beneath. The most frequent particle size is approximately 0.5 mm in all seasons. As discussed in section 2, the disdrometer struggles to detect particles less than about 0.5 mm in size, and this peak should therefore not be interpreted to mean that 0.5 is the true peak. Given the large frequency of light radar-only detected events (more on this below), it is likely that the true peak would be less than 0.5 mm. This plot demonstrates rather that small particles constitute the majority of Macquarie Island's precipitation, and the size distribution has an exponential form (above 0.5 mm).

A second notable feature of the top distribution is the seasonal tendencies of larger particles. In both fall and winter, particle sizes extend past 10 mm in size. Raindrops

generally reach sizes of 3-5 mm at most (bottom panel). Above this range, liquid drops break apart due to air drag, although the largest-recorded raindrop diameter was 8.8 mm during tropical rainfall (Hobbs & Rangno, 2004).

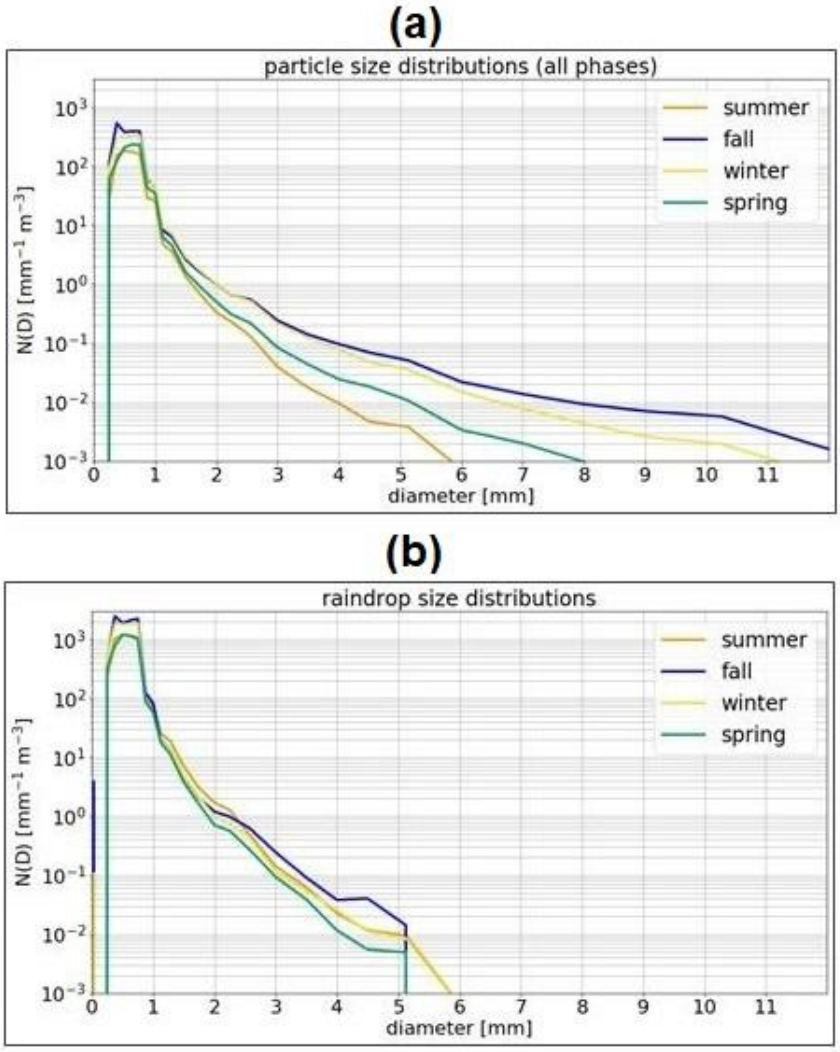

Figure 3-3 (a) Seasonally separated particle size distributions for all phases of precipitation. (b) Seasonal raindrop size distribution.

The increased presence of frozen precipitation in fall and winter are due to thermodynamic and, to a lesser extent, dynamic impacts. While subsequent sections will cover frontal precipitation in greater detail, Fig. 3.4 shows a distribution of synoptic sectors partitioned by season. Fig. 3.4 shows that fall and winter quadrants do not have significantly higher overall occurrence of frontal systems (the occurrence of "far" is about the same) or time spent in the cold-sector quadrant (NW) of low pressure systems. While Fig. 3.5 shows that frozen precipitation events do occur most often in the NW quadrant, the time spent in NW quadrants is actually lower in fall and winter than spring and summer, and we conclude

that the seasonal differences in frozen precipitation is not due having more frequent cold-frontal passages.

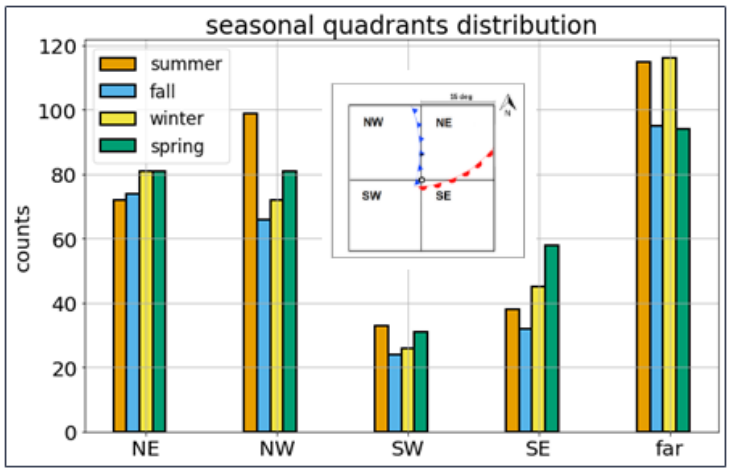

Figure 3-4 Distribution of synoptic storm quadrants, broken into seasons.

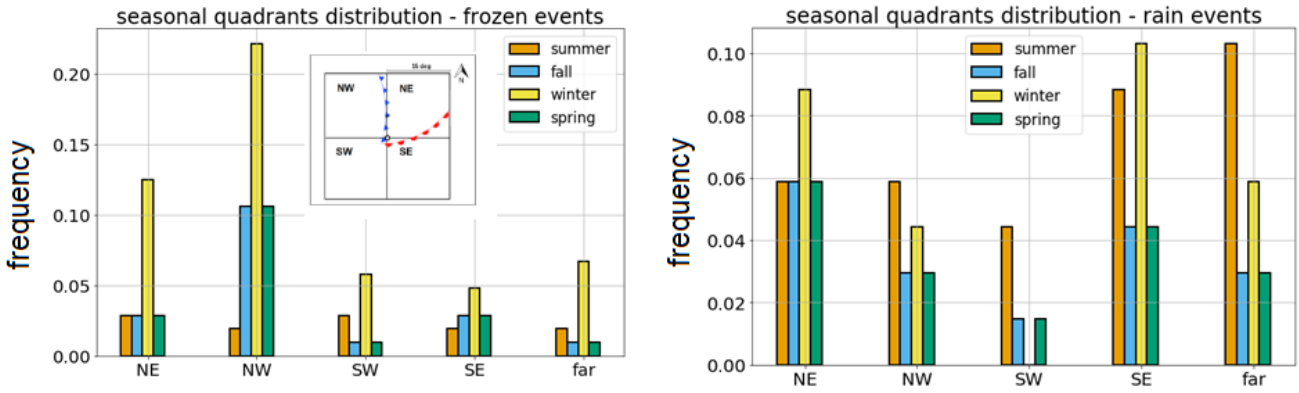

Figure 3-5 Frequency of frozen and liquid precipitation events by storm quadrant and season. The total frequency in each panel is normalized by the total number events of its phase (sum of all bars will equal 1).

Figures 3.6 and 3.7 show the seasonal change in surface air temperature and a histogram of precipitation type by surface temperature. Surface temperatures are lowest in the fall and winter (Fig. 3.6) making it more likely that frozen precipitation reaches the surface without melting, and not surprisingly Fig. 3.7 show a relatively higher occurrence of frozen precipitation and less rain for surface air temperatures less than about 4° C. Fig. 3.8 likewise shows that snow (which falls relatively slowly) occurs preferentially at the coldest temperatures. The tendency for more frequent frozen fall and winter precipitation is therefore more thermodynamic (and related to seasonally-driven changes in surface temperature) than a dynamical change in occurrence of baroclinic systems.

Figs. 3.7 and 3.8 also shows that small-particle precipitation occurs at all surface temperatures, but its median and interquartile range resemble those of rain.

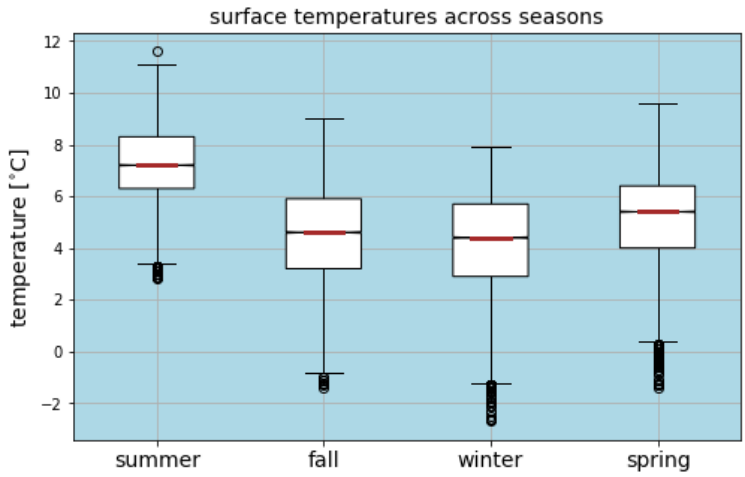

Figure 3-6 Temperatures in different seasons. The red line is median temperature, range is indicated by black vertical lines, interquartile range by rectangles, and flier values are dots.

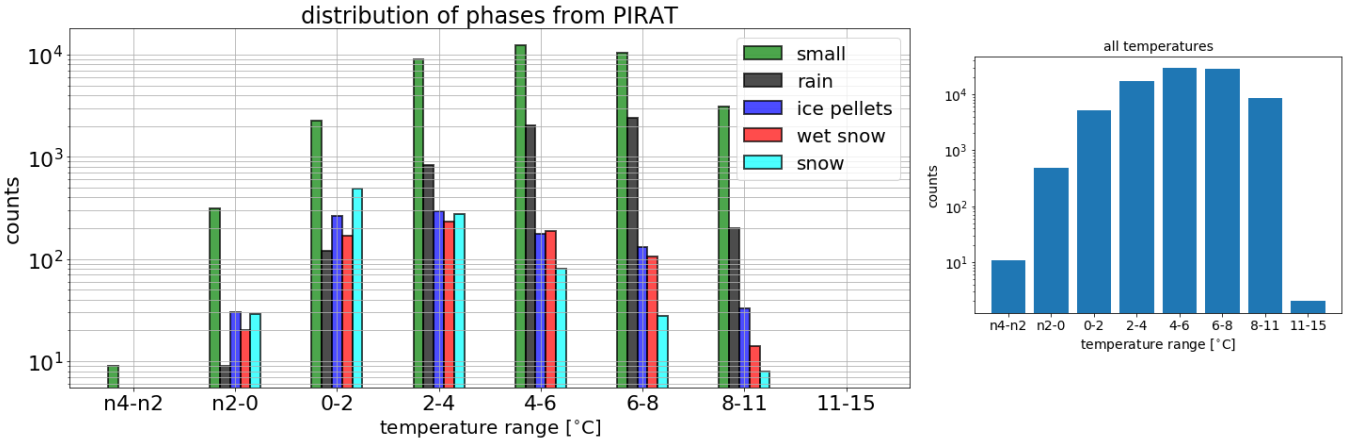

Figure 3-7 Left: Histogram of each type of precipitation binned by temperature at which it occurs. Counts indicate the entire MICRE dataset. Right: Histogram of temperature ranges from April 2016-March 2018.

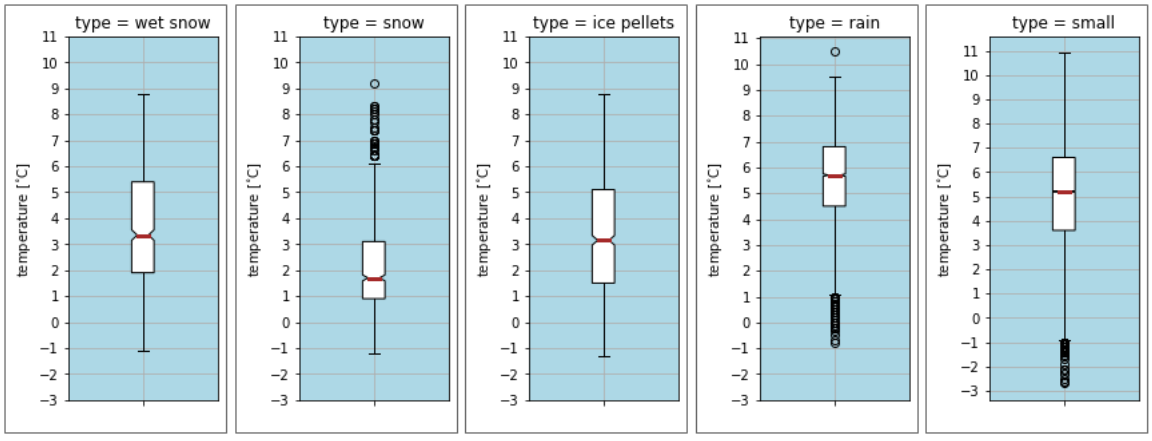

Figure 3-8 Surface temperatures plotted as in Figure 3.6 for different phases.

3.1.3 Contributions to accumulation by each phase from deep and shallow clouds

In this section we examine how precipitation type (phase) and accumulation vary depending on whether they are associated with deep- or shallow cloud systems. Figs. 3.9**a.** & 3.9**b.** show accumulation across seasons, for different precipitation classes. The depth of clouds systems (deep vs. shallow) is determined by applying a 5-minute running mean to W-band radar reflectivity profiles. Precipitation depth is inferred as the height (going up from the surface) where there is a continuous mean reflectivity signal of -15 dBZ or greater.

Deep clouds (meaning a precipitation depth > 3000 m) in Fig. 3.9**a.** show especially high accumulation from autumn frozen precipitation. Heavy rains tend to contribute the highest volume to accumulated precipitation (Fig. 3.10), except in the fall, where deep frozen accumulation surpasses rain. (Note Fig. 3.3 also shows that fall has the highest occurrence of precipitating particles larger than 5 mm). Aside from autumn, deep rain contributes the most to the overall annual accumulation. Other features of note here include drizzle, which contributes a few percent to net accumulation (note the horizontal axis here is logarithmic), and comes primarily from shallow clouds (Fig. 3.9**b.**). We also note that shallow clouds yield frozen precipitation in all seasons. This peaks in winter rather than fall, as is the case for deep frozen precipitation.

Fig. 3.10 provides the percent of volume accumulated in each season, including phase-specific contributions. Here the percent accumulations are relative to the annual overall accumulation. In all seasons, snow contributes visibly more to accumulation than other frozen types. Small-particle precipitation, while more frequent than large-particle (Fig. 3.1) contributes only a few percent to the overall accumulation. Rain contributes more to accumulation than all other types combined, especially in summer. As seen in Fig. 3.11**a**, summer has higher average rain rates. This higher summer rain rate is statistically significant, and the rates distribution also has higher extremes in summer. In a similar vein, frozen precipitation occurs at heavy rates during autumn (Fig. 3.11**b**). In general, the heaviness of

precipitation plays a larger role in the surface water budget than frequency of time that it precipitates.

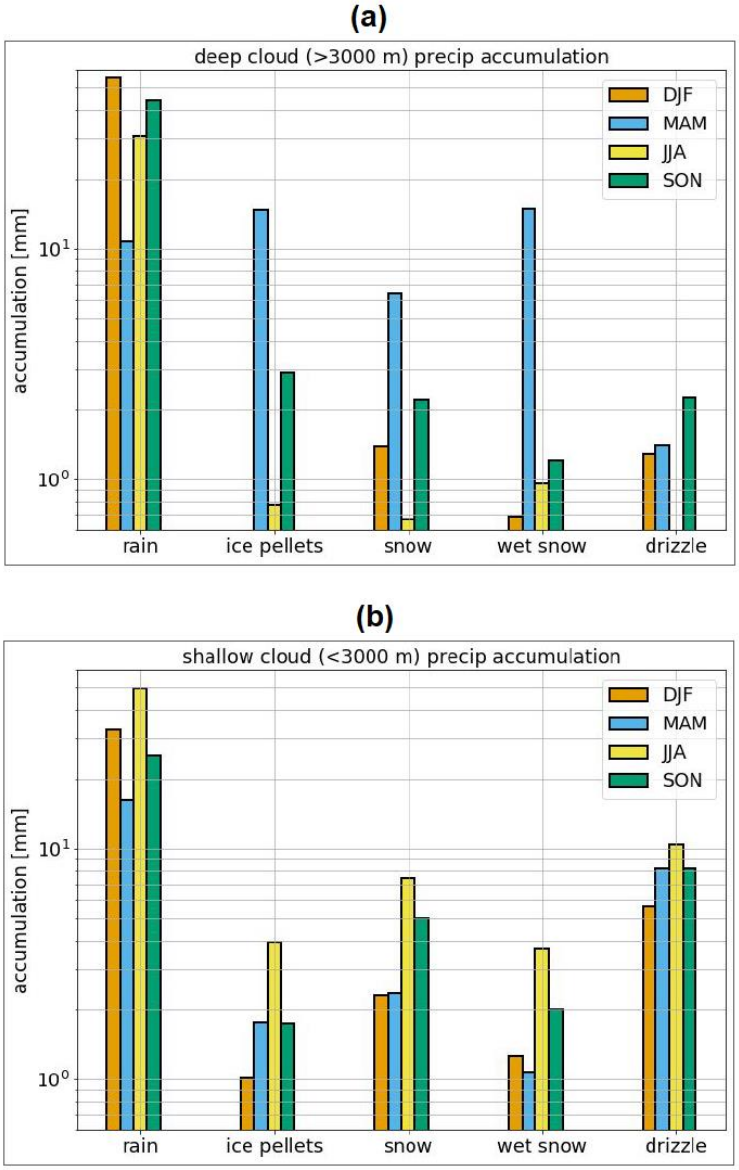

Figure 3-9 Accumulations in each season, broken into different phases for (a) deep and (b) shallow clouds.

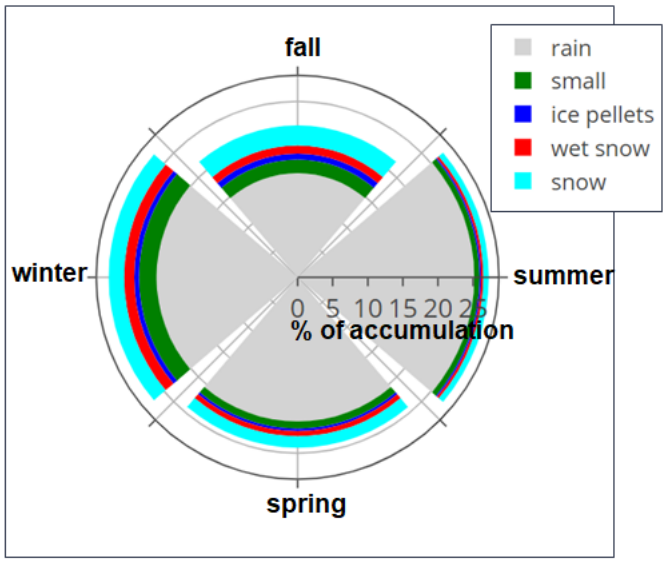

Figure 3-10 Seasonal contributions of each precipitation phase to total accumulated liquid, normalized by total annual accumulation.

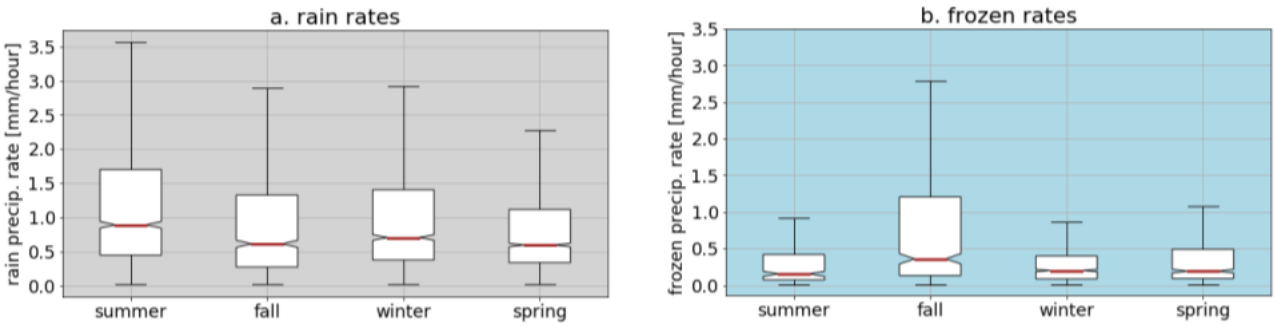

Figure 3-11 (a.) Seasonal rain and (b.) frozen rate distributions.

3.2 Synoptic environment

This section looks at precipitation characteristics surrounding MCMS storm centers, using the quadrant method. The pie chart in Fig. 3.12 shows sample sizes in different quadrants. Storms pass most frequently to the south of Macquarie Island, giving the NE and NW quadrants larger sample sizes than SE and SW.

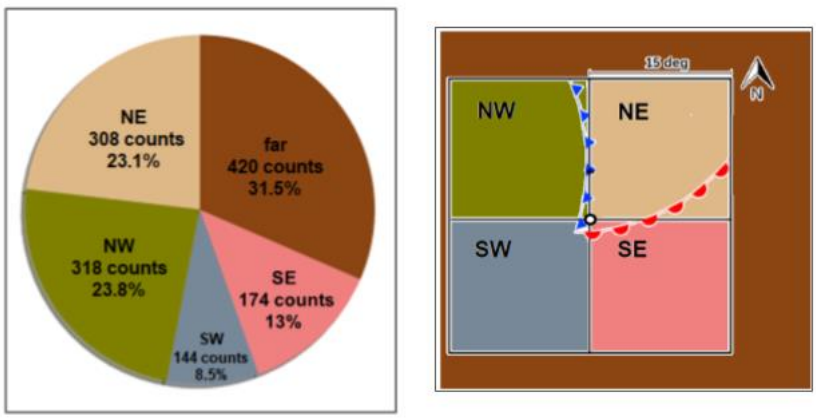

Figure 3-12 Sample sizes in different storm quadrants.

3.2.1 Precipitation characteristics by quadrant

As seen in Fig. 3.12(a), large deep-cloud accumulation results when storms pass to the SE of Macquarie, with large volume contributions from frozen precipitation. The distribution of precipitation rates from deep clouds (Fig. 3.13) shows that SE quadrant has the highest precipitation rate, while precipitation rates far from any storm or in the NE quadrant tend to be significantly lighter. The large rates in the SE quadrant likely come from the advection of moist, warm air into the SE quadrant via a warm conveyor belt (Field & Wood, 2007). Using CloudSat, SO cyclones have been observed to have their highest clouds directly east of the low (Naud et al. 2014). As eastward distance from the low and cold front increase, along the expected location of the warm front, these high clouds extend southward due to the clockwise cyclonic rotation in the SH. While surface temperatures are not as low in the SE as in the NW or SW quadrants, the median is 1^{o}C higher than the NW and SW (Fig. 3.14). The development of deep precipitation produces heavy rain and frozen precipitation, likely enhanced by seeder-feeder processes. Measurements by the tipping bucket in Fig. 3.15(a) also show that the average 6-hour accumulation is highest in the SE quadrant. In general, the SE contributes most to total accumulation.

Shallow precipitation (Fig. 3.12(b)) shows a marked increase in drizzle, and less accumulation from large-particle precipitation. The accumulation of shallow snow is largest in the NW quadrant (post-cold front sector), likely because of the thermodynamic environment – post-cold front conditions have the lowest temperatures.

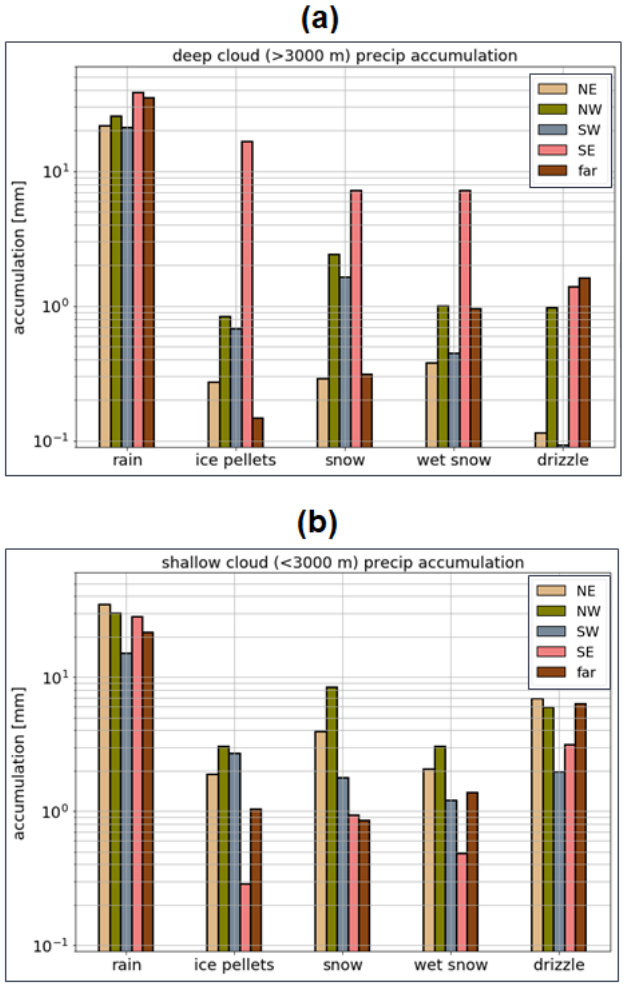

Figure 3-13 Accumulation from (a) deep and (b) shallow clouds in different sectors.

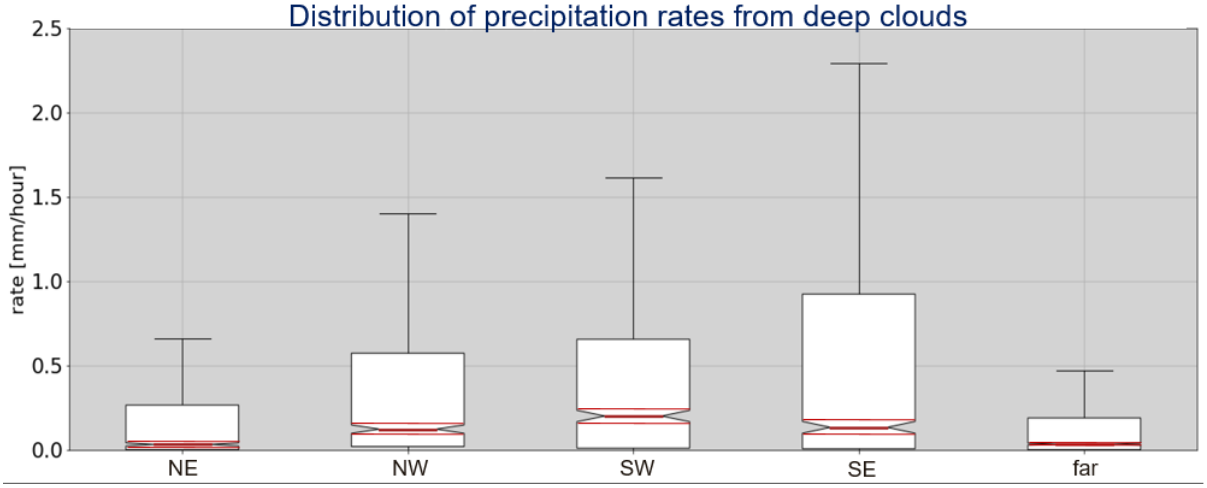

Figure 3-14 Precipitation rates in different sectors. The red line is median temperature, knotches are confidence intervals, range is indicated by black vertical lines, interquartile range by rectangles, and flier values are dots.

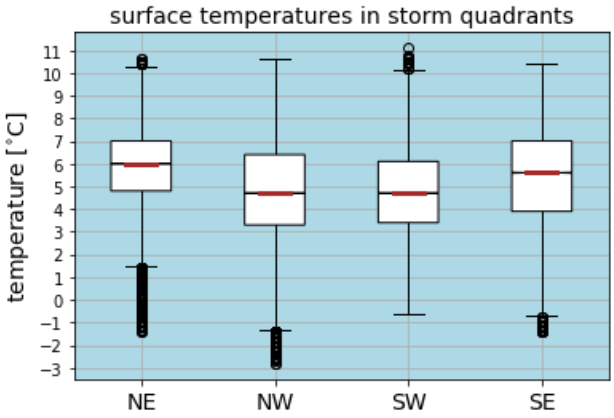

Figure 3-15 Temperatures in different storm quadrants. The red line is median temperature, range is indicated by black vertical lines, interquartile range by rectangles, and flier values are dots.

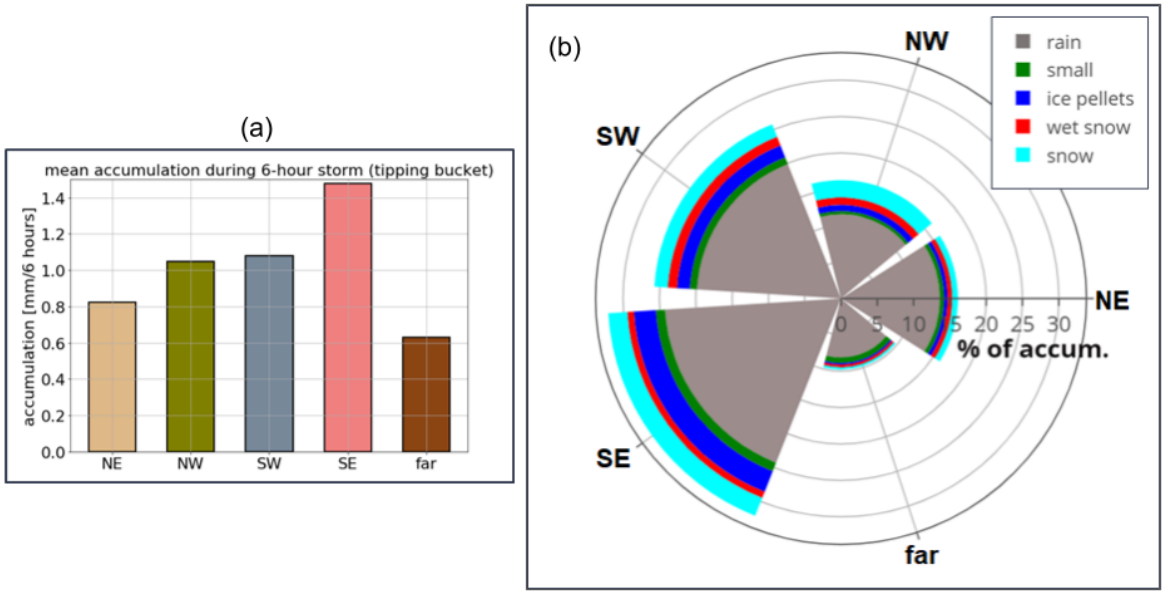

Figure 3-16 (a) Tipping bucket 6-hour accumulation during precipitation events (excludes non-precipitating). (b) Sector contributions of each precipitation phase to total accumulated liquid, normalized by total accumulation.

3.3 Diurnal cycle at Macquarie Island

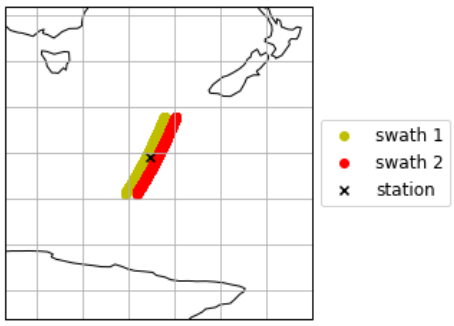

Figure 3-17 The two closest CloudSat overpasses over Macquarie (red and yellow), plotted with respect to the MICRE site (black x).

The two nearest CloudSat overpasses over Macquarie (within ±0.75°, shown in Fig. 3.16) occur at approximately 14:30 and 15:20 UTC, once every 16 days; the local time of

these overpasses is approximately 1:30 and 2:20 AM. The diurnal cycle of precipitation from our MICRE blend product is examined in this section.

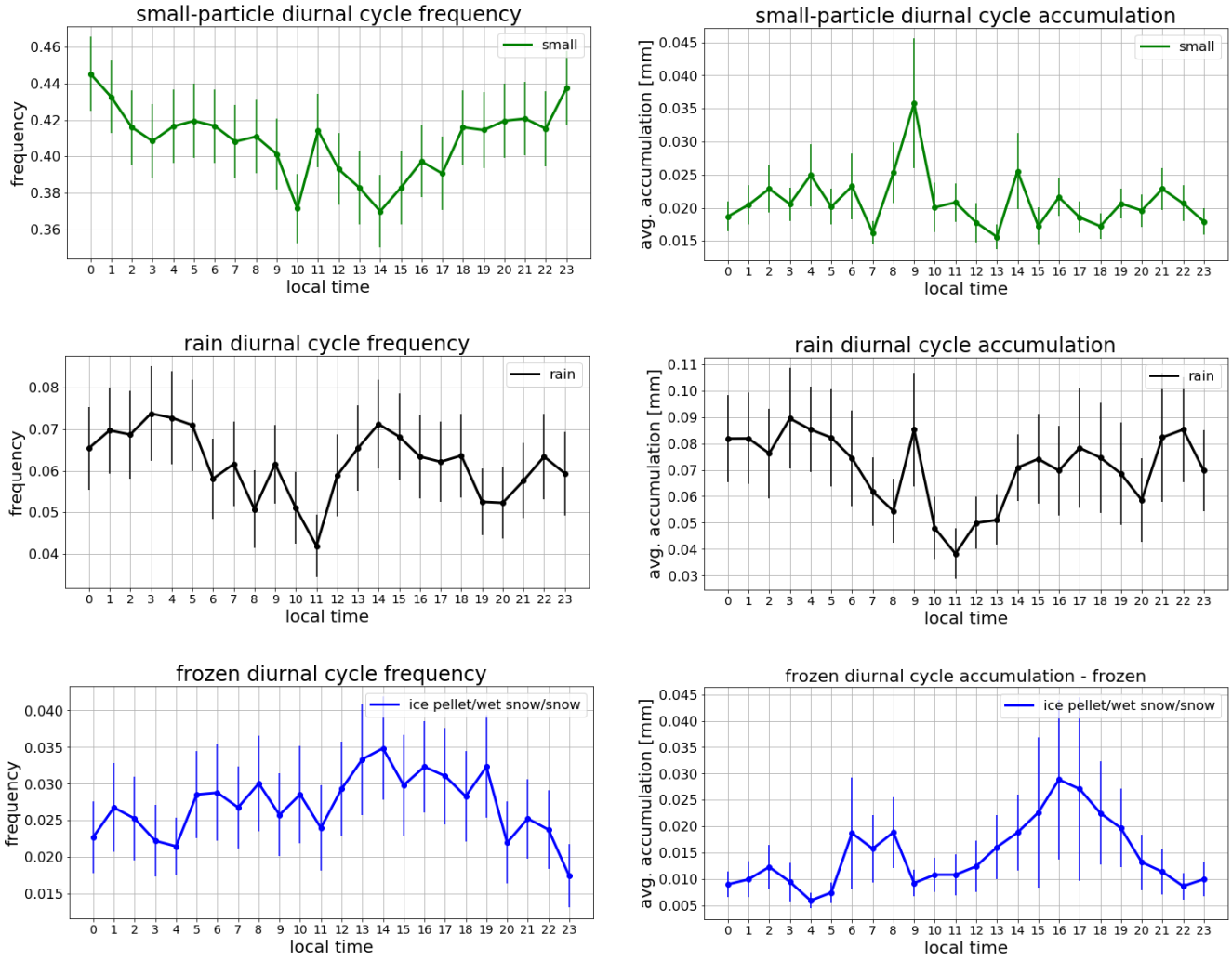

Figure 3-18: The diurnal cycle of small-particle, rain and frozen precipitation plotted as frequency of occurrence (left column) and average accumulation per hour (right column).

The diurnal frequency of occurrence and accumulation of surface precipitation grouped into small, rain and frozen categories are plotted in Fig. 3.17. In all plots, error bars show the standard error in the mean. Small-particle precipitation has relative minima between about 10:00 and 17:00 and a peak near midnight, while rain displays two modes, with a nighttime peak near 3:00 or 4:00 and an afternoon peak near 14:00. In sequence, small particle precipitation (drizzle) becomes more frequent after 14:00 and peaks near midnight, likely driven by the longwave cooling and destabilization of the boundary layer as solar heating wanes. After midnight, drizzle decreases in favor of rain for the next several hours, suggesting an increase in particles size (which is also seen as an increase in rain accumulations). After 4:00, rain decreases while small-particle (drizzle) lags the decrease in

rain until rain reaches a minimum near 9:00 or 10:00. Finally, frequency and accumulation from rain increase in early afternoon until 19:00 to 20:00, not preceded by an increase in drizzle, in this case.

Frozen precipitation is a topic of interest since both thermodynamic and dynamic environments facilitate glaciation. Afternoon through early evening have the highest frequency of occurrence; although these are the warmest times of day, we speculate that the instigation of secondary icing processes due to turbulence and updrafts in shallow clouds may be a factor, and as part of future work we plan to examine the dependence on cloud top, and general seasonal variations in the diurnal cycle.

Chapter 4 Ground-based comparison to CloudSat

4.1 Melting layer characteristics

Melting layers are identified with the radar by calculating dv_z/dh, the Doppler velocity-height gradient weighted by reflectivity as described in section 2.3.2. Fig. 4.1 shows a histogram of melting layer heights and a gamma-fitted curve from which the median and distribution width can be seen more clearly. The distribution illustrates that over Macquarie Island, near-surface melting layers occur frequently. Surface clutter prevents CloudSat from detecting clouds and precipitation for approximately the first 750 m above the surface (Marchand et al. 2008), a threshold which is remarkably close to the median melting layer of 751.5 m at Macquarie. The absolute frequency of occurrence of melting layers and the fraction that are below 750 are shown in Table 1. Roughly 65% of melting layers in all seasons except summer (DJF) fall below 750 m. Consequently, one might be concerned about the impact this has on CloudSat retrievals.

CloudSat snowfall estimation relies on ancillary freezing level input from ECMWF. Fig. 4.2 contains a similar gamma-fit histogram of freezing levels over Macquarie Island. The results shown here are for a grid size of $2^o \times 2^o$ during years 2006-2018 and include freezing levels for only those points where CloudSat identifies precipitation is present, regardless of whether it is rain (certain, probable or possible), mixed phase or snow. The distributions in Figs. 4.1 & 4.2 have similar features, with the median ECMWF freezing level falling at 742.7 m. In short, while CloudSat is not always able to detect the melting layer, the retrieval algorithm nonetheless appears to have a reasonable knowledge of where the freezing level is located and this information is used in the retrieval.

Table 1 Radar melting layer frequencies by season.

season	% of time there's a ML	% of time it's below 750 meters
DJF	16.8	8.2
MAM	14.9	9.7
JJA	17.3	10.9
SON	20.0	12.6

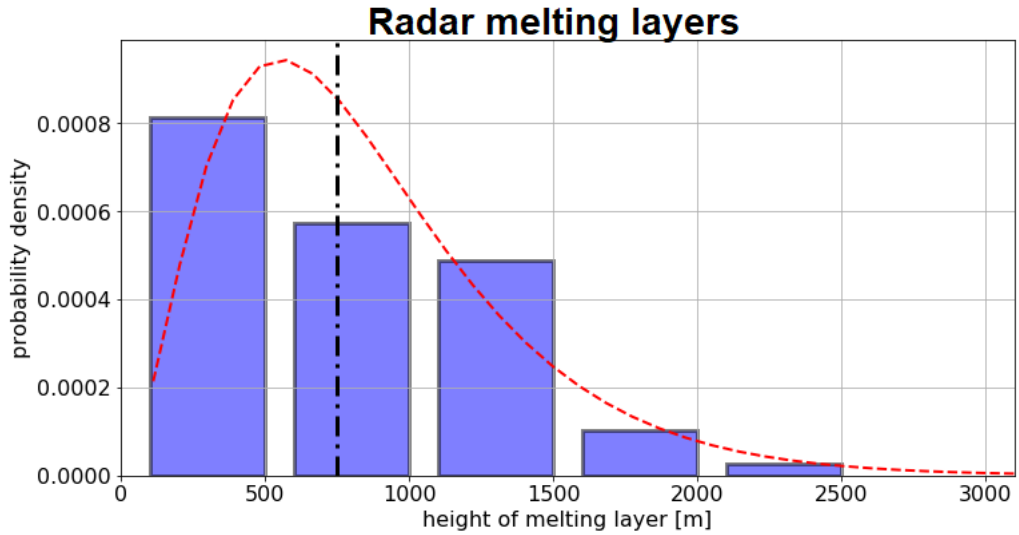

Figure 4-1 Gamma-fitted probability distribution function (red dashed line) of melting layer heights. α=2.87, β=295.47, median height = 751.5±4.8 m (black dashed line)

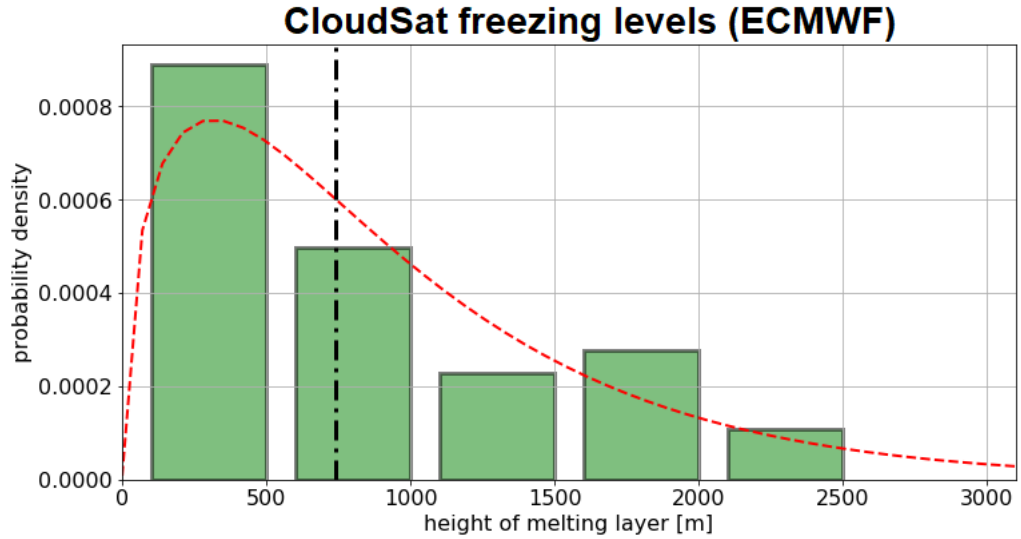

Figure 4-2Gamma-fitted (red dashed line) ECMWF freezing levels corresponding to CloudSat precipitation retrievals (rain, mixed and snow). α=1.5, β=625.3, median height = 742.7±12 m (black dashed line)

4.2 CloudSat precipitation profiles

In this subsection, I first examine CloudSat Precip-Column outputs at different spatial and temporal resolutions for the purpose of understanding how spatially variable CloudSat

retrievals are over the SO. This can be used to make a statement on how generalizable the Macquarie Island data are to the larger SO.

4.2.1 Space and time variability in the 2C-Precip-Column product

We examine whether the Macquarie Island time series, limited to a single site, represent the SO by comparing these data with CloudSat retrievals at a variety of resolutions. Specifically, resolution is lowered *(i)* in space from $10^o \times 10^o$ to $2^o \times 2^o$ for years 2006-2018, and *(ii)* in time from 2006-2018 to 2016-2018 (MICRE duration) at $10^o \times 10^o$. We focus on *(i)* phase-specific frequency of occurrence and *(ii)* rain rate. Both parameters are split into seasons. Rain rate incorporates only data flagged as "rain certain", "rain probable" or "rain possible." Precipitation rates for mixed phase or snow data will be examined in future work using the 2C-Snow-Profile.

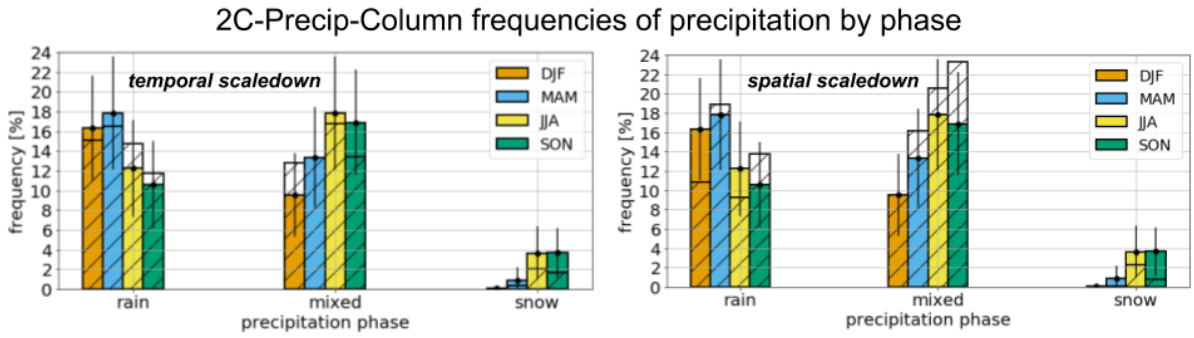

Figure 4-3

Fig. 4.3 shows the results of these temporal and spatial scaledowns. The frequency plots contain the reference frame (color bars; $10^o \times 10^o$, 2006-2018) compared to the scaledown (hatched bars), with black vertical lines showing standard error of the reference mean. The temporal scaledown shows no significant differences (without the uncertainty bars) during the years of the MICRE project (2016-2018) compared to all-years data, and consequently we conclude that the two years of MICRE are typical of the CloudSat dataset. Frequency plots at higher spatial resolution, however, show there is significantly less summer rain, more spring mixed phase, and less spring snow in the small ($2^o \times 2^o$) region than over the larger $10^o \times 10^o$ (reference) results. We conclude that Macquarie data cannot be used to

represent the entire $10^o \times 10^o$ region. We examine the spatial variability further in Fig 4.4, where we break the $10^o \times 10^o$ box into three latitudinal bands. A similar analysis was performed for the west, middle and east thirds, but no significant longitudinal differences were observed. However, significant differences in SO precipitation retrievals emerge as a function of latitude. In Fig. 4.4, bars overlaid in hatching are for the $2^o \times 2^o$ box over Macquarie and colored bars are the varied zonal bands (for 10^o of longitude). The southernmost band has significantly more summer and fall mixed, and winter and spring snow. In the northernmost band, the frozen-phase differences transition visibly to rain, across all seasons. CloudSat's sensitivity to precipitation phase is thus heavily influenced by zone.

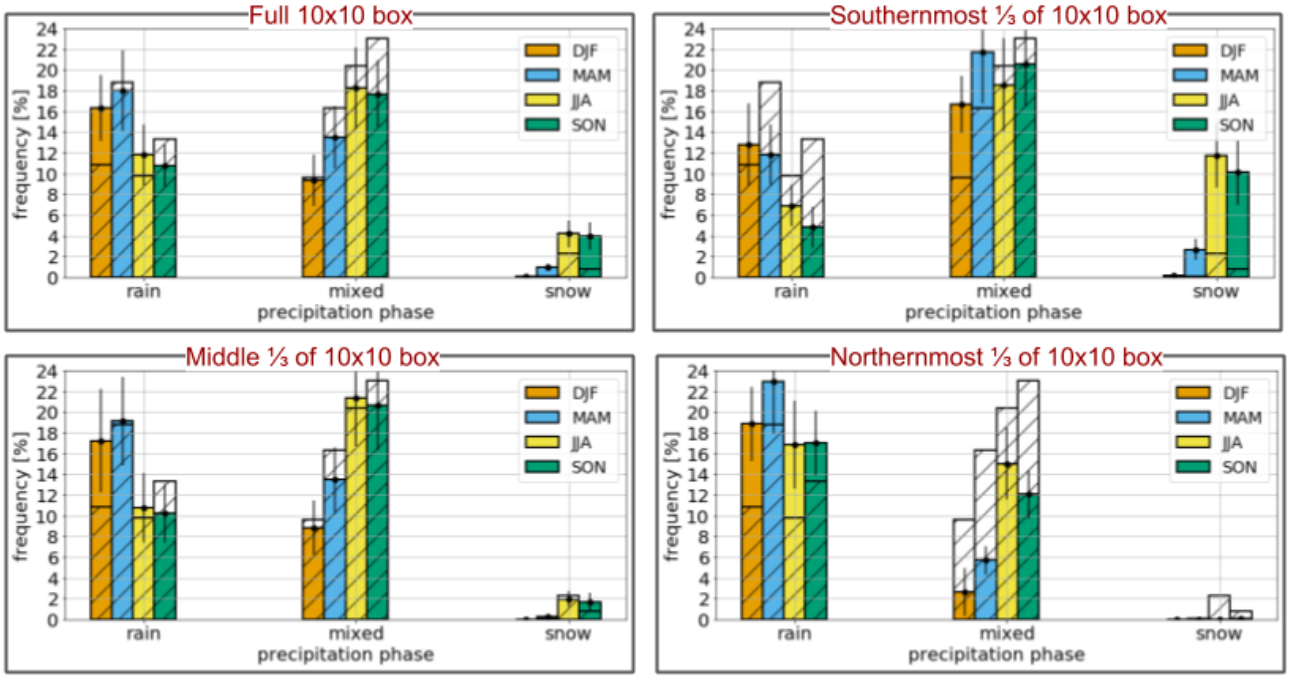

Figure 4-4

4.2.2 MICRE blend-CloudSat comparison

The Precip-Column data contains rates retrieved for certain, probable and possible instances of rain. The various precipitation flags, plotted in Fig. 4.5, signify the different levels of certainty in the retrieval. In the "rain possible" cases, hydrometeor reflectivity is generally low and rates are light. Fig. 4.5 also shows the percent of time that mixed precipitation and snow are certain and possible. The pie chart is comprised of precipitation flags for all 2006-2018 overpasses contained in a $3.3^{o}\times3.3^{o}$ box over Macquarie.

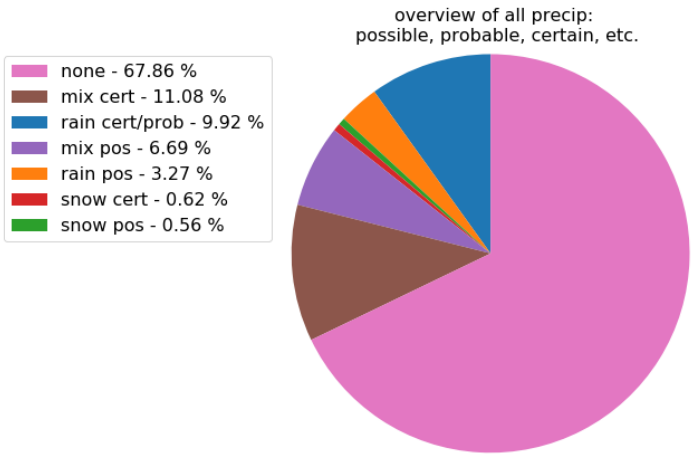

Figure 4-5

The histograms shown in Fig. 4.6 compare the total percentage of time that CloudSat and the MICRE blend contain frozen (both snow and mixed; left plot) and no precipitation (right). For the CloudSat data, this is plotted using the 3.3^{o} longitude centered on Macquarie, and the three 3.3^{o} latitude bands described in Section 4.2.1. Error bars show the standard error of the mean. Fig. 4.6 (left) shows a comparison between MICRE frozen (snow/wet snow/ice pellets) and CloudSat frozen precipitation (snow/mixed; these are combined into one overarching category of "frozen").

As evidenced by the pie chart, CloudSat classifies precipitation as mixed phase significantly more frequently than the blend's equivalent, "wet snow," and is likely overestimating the amount. Although CloudSat's freezing level input from ancillary data resemble the MICRE melting layer distribution (Figs. 4.1 & 4.2), the amount of partially-frozen precipitation is significantly higher according to the satellite vs. ground-based observations.

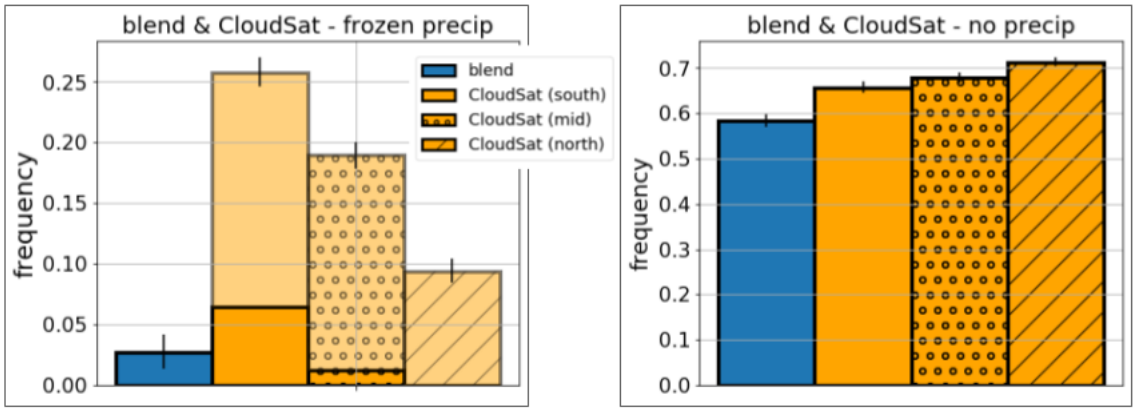

Figure 4-6 Frequency (fraction of time) that frozen (left; light orange: "snow/mixed possible"; dark orange bars: "snow/mixed certain.") and no precipitation (right) are observed, according to the MICRE blend and CloudSat. CloudSat is broken into the northernmost, middle and southernmost thirds of the 10^o latitude span over Macquarie; the longitude is 3.3^o centered on Macquarie.

The second set of histograms, Fig. 4.7, show rain rates for the three CloudSat latitude bands in comparison to the MICRE blend. CloudSat's sensitivity limits rates to a minimum of 0.009 mm/hour, but in the case of the MICRE blend, rates lower than this are evident. These light rates correspond to the PIRAT phase class "small" (green bars), which transitions to the "rain" class (black bars) as rates get higher on the histogram. Thus, the CPR misses this light precipitation comprised of small particles. This results in a higher frequency of "no precipitation" by CloudSat, as seen in Fig. 4.6. Moderate-to-heavy rates (0.5 mm/hour and upward), however, match well between the satellite and ground. Taking error bar ranges into account, no significant differences emerge between the blend and CloudSat for rates above 0.5 mm/hour. The satellite observes SO precipitation above this threshold with a high degree of accuracy.

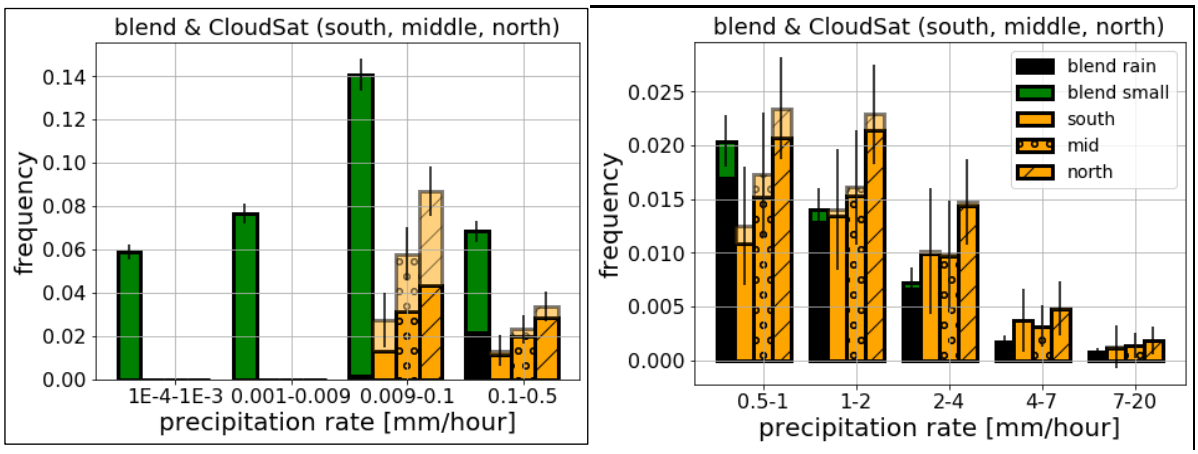

Figure 4-7 Rates histograms plotted on separate axes for visibility. CloudSat rates are plotted separately for different latitude bands, as in Fig. 4.6. Blend rates are separated into small- (green) and large-particle rain (black).

Chapter 5 Summary and discussion

Ground-based precipitation observations suggest that episodes with high rain rates contribute substantially to the SO water budget. From a seasonal perspective, heavy rains occur year-round but occur most often in summer. Frozen and partially-frozen precipitation contributes substantially more to the total water in fall and winter than other seasons. This characteristic is consistent with fall and winter having lower median surface temperatures, which occur in fall and winter and are statistically significant at the 95% confidence level. Ultimately we find seasonal thermodynamic variations more important than dynamical variations in frontal passages, regarding variation in frozen precipitation. As part of future work, we plan to study how variations in cloud properties and in-cloud microphysical processes are related to the variations in precipitation characteristics we have identified here.

While thermodynamics play a large role in shaping the phase of surface precipitation, large-scale dynamics remain critical, influencing both SO precipitation rates and phases. Instances of deep frozen precipitation are observed to occur most often when Macquarie is southeast of cyclone systems. Nonetheless, precipitation (including frozen precipitation) occurs far from frontal systems and contributes significantly to total precipitation. Much remains to be learned about the interaction between precipitation, cloud, aerosols and radiation.

Examination of CloudSat retrievals shows that it is necessary to focus on a relatively narrow latitudinal band when doing comparisons with surface observations. Overall, we find that CloudSat retrievals compare well with our surface data for rain rates above 0.5 mm/hour rates for liquid precipitation (rain). CloudSat is unable to identify much of the light drizzle reaching the surface at lower rain rates, however, this light rain only accounts for a fairly small amount of the total accumulation. Nonetheless, the light precipitation is widespread and amost certainly plays a critical role in modulating cloud, aerosol and radiative properties in the region. A limitation of this analysis is that we have not analyzed the phase of the small

precipitating particles that make up the bulk of the preicpitation missed by CloudSat. Analysis by Mace & Protat (2018) based on lidar depolarization suggest this precipitation is primarily liquid. We hope the processing of MICRE lidar data will be completed in the near future and can be incoporated in our anaysis as part of future work. We plan to evaluate frozen precipitation in more detail as part of future work, but preliminary results suggest that CloudSat overestimates the occurrence of mixed-phase precipitation.

Bibliography

Adams, N. (2009). Climate trends at Macquarie Island and expectations of future climate change in the sub-Antarctic. Pap. Proc. Roy. Soc. Tasmania, 143, 1(8).

Albrecht, B. (1993). Effects of Precipitation on the Thermodynamic Structure of the Trade Wind Boundary Layer. J. Geophys. Res, 98, 7327-7337

Austin, P. M., Bemis, A. C. (1949). A quantitative study of the "bright band" in radar precipitation echoes. J. Meteor., 7, 145-151 https://doi.org/10.1175/1520-0469(1950)007<0145:AQSOTB>2.0.CO;2

Battaglia, A., E. Rustemeier, A. Tokay, U. Blahak, C. Simmer. (2010). Parsivel snow observations: A critical assessment. J. Atmospheric Ocean. Technol, 27, DOI: 10.1175/2009JTECHA1332.1

Bauer, M.P., G. Tselioudis, and W.B. Rossow, 2016: A new climatology for investigating storm influences in and on the extratropics. J. Appl. Meteorol. Climatol., 55, no. 5, 1287-1303, doi:10.1175/JAMC-D-15-0245.1.

Behrangi, A., G. Stephens, R. F. Adler, G. J. Huffman, B. Lambrigtsen, and M. Lebsock (2014). An Update on the Oceanic Precipitation Rate and Its Zonal Distribution in Light of Advanced Observations from Space. J. Climate, 27, 3957–3965, https://doi.org/10.1175/JCLI-D-13-00679.1.

Behrangi, A., M. Christensen, M. Richardson, M. Lebsock, G. Stephens, G. Hu man, D. Bolvin, R. Adler, A. Gardner, B. Lambrigtsen, E. Fetzer (2016). Status of high-latitude precipitation estimates from observations and reanalyses. Geophys. Res. Atmos., 121, 4468-4486, doi:10.1002/2015JD024546.

Bodas-Salcedo, A., P.G. Hill, K. Furtado, K.D. Williams, P.R. Field, J.C. Manners, P. Hyder, and S. Kato. (2016). Large Contribution of Supercooled Liquid Clouds to the Solar Radiation Budget of the Southern Ocean. J. Climate, 29, 4213-4228, https://doi.org/10.1175/JCLI-D-15-0564.1

Chubb, T. H., J. B. Jensen, S. T. Siems and M. J. Manton. (2013). In-situ observations of supercooled liquid clouds over the Southern Ocean during the HIAPER Pole-to-Pole Observations campaign. Geophys. Res. Lett. 40, 5280-5285, doi:10.1002/grl.50986

Friedrich, K., S. Higgins, F.J. Masters, and C.R. Lopez. (2013). Articulat-ing and Stationary PARSIVEL Disdrometer Measurements in Conditions with Strong Winds and Heavy Rainfall. J. Atmos. Oceanic Technol., 30, 2063{2080, https://doi.org/10.1175/JTECH-D-12-00254.1

Frisch, A. S., C. W. Fairall, and J. B. Snider, 1995: Measurement of stratus cloud and drizzle parameters in ASTEX with a Ka-band radar and a microwave radiometer. J. Atmos. Sci., 52, 2788–2799.

Gunn, R. and G.D. Kinzer, 1949: The terminal velocity of fall for water droplets in stagnant air. J. Meteor., 6, 243{248, https://doi.org/10.1175/1520-0469(1949)006<0243:TTVOFF>2.0.CO;2

Haynes, J. M., T. S. L'Ecuyer, G. L. Stephens, S. D. Miller, C. Mitrescu, N.

Wood, S. Tanelli. (2009). Rainfall retrieval over the ocean with spaceborne W-band radar. J. Geophys. Res., 114, D00A22, doi:10.1029/2008JD009973.

Hobbs, P. V., Rangno, A. L. (2004). Super-large raindrops. Geophysical Research Letters, 31, doi:10.1029/2004GL020167.

Hewson, T.D. (1998). Objective fronts. Met. Apps, 5: 37-65. doi:10.1017/S1350482798000553

Huang, Y., S.T. Siems, M.J. Manton, D. Rosenfeld, R. Marchand, G.M. Mc-Farquhar, A. Protat. (2016). What is the Role of Sea Surface Temperature in Modulating Cloud and Precipitation Properties over the Southern Ocean. J. Climate, 29, 7453{7476, https://doi.org/10.1175/JCLI-D-15-0768.1

Jiang, J. H., Wu, D. L. (2004) Ice and water permittivities for millimeter and sub-millimeter remote sensing applications. ASL, https://doi.org/10.1002/asl.77

Kay, J.E., C. Wall, V. Yettella, B. Medeiros, C. Hannay, P. Caldwell, C. Bitz. (2016). Global Climate Impacts of Fixing the Southern Ocean Shortwave Radiation Bias in the Community Earth System Model (CESM). J. Climate, 29, 4617{4636, https://doi.org/10.1175/JCLI-D-15-0358.1

Kollias, P. and B. Albrecht. (2005). Why the melting layer radar reflectivity is not bright at 94 GHz. Geophysical Research Letters, 32, L24818-L24822, doi:10.1029/2005GL024074

Lang, F., Huang, Y., Siems, S. T., Manton, M. J. (2018). Characteristics of the marine atmospheric boundary layer over the Southern Ocean in response to the synoptic forcing. Journal of Geophysical Research: Atmospheres, 123, 7799|7820. https://doi.org/10.1029/2018JD028700

Löffler-Mang, M., Joss, J., (2000). An Optical Disdrometer for Measuring Size and Velocity of Hydrometeors. J. Atmos. Oceanic Technol. 17 (2): 130–139. https://doi.org/10.1175/1520-0426(2000)017<0130:AODFMS>2.0.CO;2

Mace, G.G., and A. Protat, 2018: Clouds over the Southern Ocean as observed from the R/V Investigator during CAPRICORN: Part I: Cloud occurrence and phase partitioning, J. Appl. Meteor. Clim., 57, 1783-1804, doi:10.1175/JAMC-D-17-0194.1.

Mitrescu, C., T. L'Ecuyer, J. Haynes, S. Miller, and J. Turk, 2010: CloudSat Precipitation Profiling Algorithm/Model Description. J. Appl. Meteor. Climatol., 49, 991{1003, https://doi.org/10.1175/2009JAMC2181.1

Morrison, H. and A. Gettelman, 2008: A New Two-Moment Bulk Stratiform Cloud Microphysics Scheme in the Community Atmosphere Model, Version 3 (CAM3). Part I: Description and Numerical Tests. J. Climate, 21, 3642–3659, doi: 10.1175/2008JCLI2105.1

Naud, C.M., D.J. Posselt, and S.C. van den Heever, 2015: A CloudSat-CALIPSO view of cloud and precipitation properties across cold fronts over the global oceans. J. Climate, 28, no. 17, 6743-6762, doi:10.1175/JCLI-D-15-0052.1.

Orr, B. W., and R. A. Kropfli, A method for estimating particle fall velocities from vertically pointing Doppler radar, J. Atmos. Oceanic Technol., 16, 29–37, 1999.

Stephens, G. L., J. Li, M. Wild, C. A. Clayson, N. Loeb, S. Kato, T. L'Ecuyer, P. W. Stackhouse Jr, M. Lebsock, and T. Andrews. (2012). An update on Earth's energy balance in light of the latest global observations. Nature Geoscience, 5, 691-696, DOI: 10.1038/NGEO1580

Skofronick-Jackson, G., S. Munchak, M. Kulie, L. Milani, N. Wood, G. Huffman. (2018). The GPM mission status: Emphasis on falling snow retrievals. IEEE International Geoscience and Remote Sensing Symposium, DOI: 10.1109/IGARSS.2018.8519544

Simmonds, I., Keay, K., Bye, J. (2012). Identification and Climatology of Southern Hemisphere Mobile Fronts in a Modern Reanalysis. Journal of Climate. 25. 1945-1962. 10.1175/JCLI-D-11-00100.1.

Trenbarth, K. and J. Fasullo. (2010). Simulation of present-day and twenty-first century energy budgets over the Southern Ocean. J. Climate, 23, 440-454, DOI: 0.1175/2009JCLI3152.1

von Lerber, A., D. Moisseev, D.A. Marks, W. Petersen, A. Harri, and V. Chandrasekar, 2018: Validation of GMI Snowfall Observations by Using a Combination of Weather Radar and Surface Measurements. J. Appl. Meteor. Climatol., 57, 797-820, https://doi.org/10.1175/JAMC-D-17-0176.1

Wang, Z., D. Belusic, M. Manton, and Y. Huang. (2015). A climatology of the precipitation over the Southern Ocean as observed at Macquarie Island. J. Appl. Meteorol. Climatol, 54, 2321-2337, doi:10.1002/grl.50986

Appendices

Appendix I.
Parsivel **I**mproved **R**ate **a**nd **T**ypes (PIRAT) algorithm
This document describes the PIRAT algorithm subroutines. Data output by the Parsivel vendor's proprietary algorithm serve as raw input. Input is subjected to secondary processing and statistical analysis to improve the accuracy of particle thermodynamic phase identification. Subsequent microphysical calculations include precipitation rate, effective radius and particle size distributions (PSD).

A. change_resolution($t, R_{pars}, H_{raw}, A, v_{rawfall}, D, d_x$)

'change_resolution' first identifies any missing timesteps to create a complete 1-minute resolution daily array (length=1440). Empties are assigned to periods of missing data. Then d_x is used to decrease the resolution of H_{raw}. For results shown in this work, spectral resolution was decreased from 1 to 5 minutes.
Decreasing spectral resolution benefits the analysis by enabling more counts to accumulate, giving the 5-min spectrum a characteristic shape indicative of the falling precipitation's thermodynamic phase (see next subroutine).

Input for this subroutine includes the timestamps and raw laserband amplitude arrays, plus level 2 processed output by the Parsivel vendor retrieval:

- H_{raw} - 'spectrum_array,' observed particle size-velocity histogram;

  dimensions: (t, $v_{rawfall}$, D); unit: counts

  t = 1-minute time array; unit: seconds

  $v_{rawfall}$ = raw fall velocity (32 bins, unit: m/s)

  D = effective particle diameter (32 bins, unit: mm)

- R_{pars} - 'precip_rate' from the vendor's retrieval

  dimension: t; unit: mm/hour

- A_{laser} - 'laserband_amplitude'

  dimension: t; unit: arbitrary counts

- d_x - 'divisorx' - integer divisor to be used to decrease 1-minute spectral resolution to e.g. 5-minute resolution

Output returned by 'change_resolution':

- H_{xmin} - 'rawspecxmin' - using H_{raw}, x-minute resolution size-velocity spectra are binned. Note: for this work, x=5.

  dimensions: (t_x, $v_{rawfall}$, D); units: counts

- t_x = x-minute timesteps (e.g. 288 for 5-min res.)

  dimension: t/d_x; units: seconds

- $t_{missing}$ = Parsivel's 'time' array with NANs in places where the instrument cut out

  dimension: $t_{missing}$; units: seconds

- $R_{pars}^{missing} = R_{pars}$ array with zeros in places where the instrument cut out

  dimension: $t_{missing}$; units: mm/hour

  Note: R_{pars} isn't used in any PIRAT subroutines but is plotted in results to compare to PIRAT's performance.

- DQ = data quality flag aray

  dimension: t_x

  bit 1 = 'missing_all_spectra' means all spectra (x-min resolution) are missing due to instrument issues; histogram of zeros was added to pad missing time

  bit 2 = 'missing_n_of_x_spectra' means out of x minutes, a number of measurements are missing

  bit 3 = 'renormalized' before calculations (PSD, effective diameter, rate). Counts from noise regions are added to median bins (not applicable to this subroutine; see 'rates_calculation').

- $A_{laser}^{missing} = A_{laser}$ with NANs in places where the instrument cut out

  dimension: $t_{missing}$

B. specshift

This subroutine applies an upward velocity shift dv to counts in 5-minute resolution histograms. Shifting populated bins upward on the velocity axis is mainly done to prevent windy conditions from compromising vertical fall speeds; however, very low correlation between wind speed, wind direction and the "spectral blurring" effect was found.
Regardless, a horizontal velocity component can result from high winds or near-surface turbulent gusts. This compromises the retrieved hydrometeor vertical velocity component, resulting in too-low fall speeds.
'specshift' identifies which spectra are candidates for velocity shifts by considering counts in the noise regions of a spectrum (Fig. 1). The algorithm (schematic shown in Fig. 2) takes the following into account:
(*i*) large (likely frozen or partially frozen) particles falling at reasonable speeds → no shift applied, as spectrum is likely frozen precipitation;
(*ii*) high counts in the histogram bins corresponding to snow → no shift applied, as spectrum is likely frozen precipitation;
(*iii*) **a.** counts show up in the margin fallers region (¿0.1% of whole spectrum's counts)
b. <u>either</u> ≥ 3 counts in wind noise region, <u>or</u>
c. <20 counts in snow region
a. + **b.** or **a.** + **c.** → shift applied, as spectrum is likely liquid precipitation.

B.1. Margin faller spectral noise

This hypothesis hinges on the logic that liquid precipitation results in high occurrence of 'margin fallers,' i.e., particles that don't pass through the full laserbeam-defined cross section. This can result from splashing against the Parsivel laser/detector covers. They appear on the histogram as unrealistically small and fast (Fig. 1).

B.2. Wind-induced spectral noise

Similarly, particles with high horizontal velocity are measured as too slow, thereby defining the 'wind noise' region. The wind criterion is used to deduce when particles are likely liquid or mostly melted, but falling slower than they would in reality under the absence of wind. For comparison, the raindrop terminal fall speed v_{GK} [Gunn & Kinzer, 1949] is plotted in Fig. 1 (gold curve).

$$v_{GK} = 9.65 - 10.3 \cdot e^{-0.6 \cdot D} \tag{1}$$

in m/s, where D is the particle diameter for droplets in stagnant air.

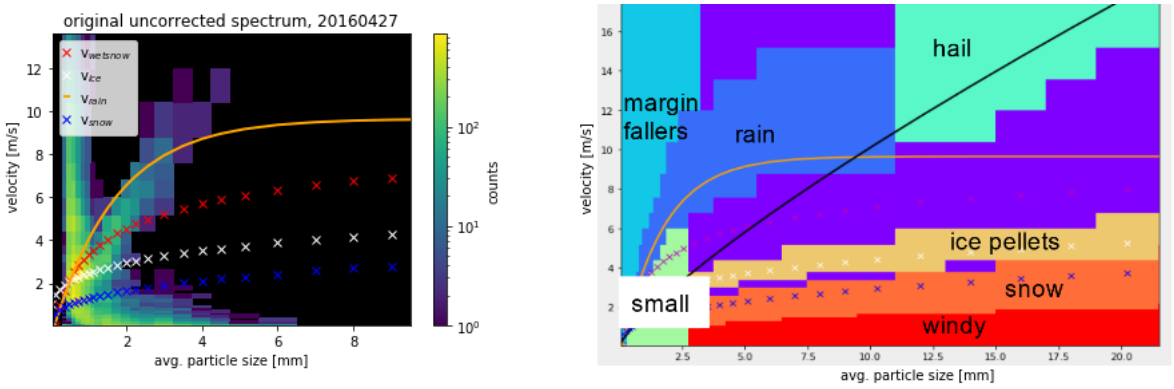

Figure 1: left: Full day raw histogram as measured by the Parsivel on a day with only warm drizzle and rain events. Non-noise counts fall below the rain terminal fall curve $v_{rain} = v_{GK}$, indicating that a shift is necessary. **right:** Defined regions of the histogram spectrum referenced in 'shiftspec' subroutine.

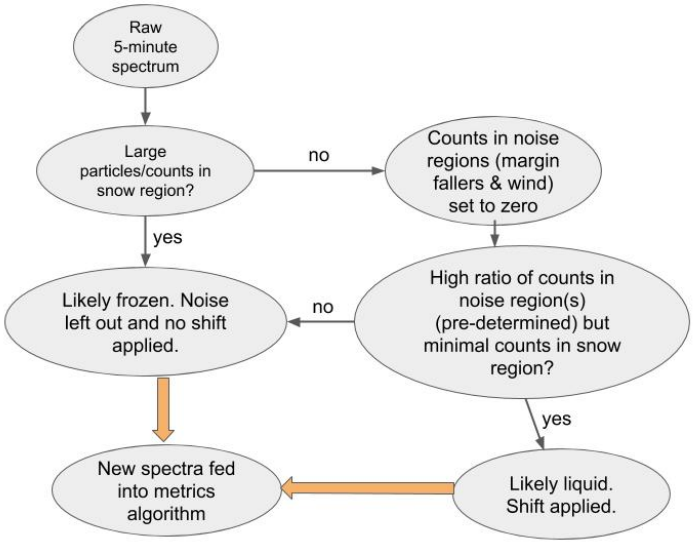

Figure 2: Schematic of 'shiftspec' subroutine.

B.3. Upward shift dv for precipitation falling too slowly

The applied dv shift is not a direct function of the horizontal wind component, as very low correlation was observed between windspeed and retrieved rain fall speed errors. This can be seen in the scatterplots in Fig. 3. The scatterplot colorbars also

show normalized probability density of finding counts at that particular location on the dv vs. wind speed axes.
An increase on the dv-axis for maximum probability density (yellow regions) occurs as hydrometeor diameter increases. dv is therefore expressed as a function of hydrometeor diameter (Fig. 4):

$$dv = p_0 + p_1 \cdot D + p_2 \cdot D^2 + p_3 \cdot D^3 \tag{2}$$

$$[p_3, p_2, p_1, p_0] = [\text{-}0.157,\ 1.255,\ \text{-}1.968,\ 2.905]$$

The average difference between *observed* fall velocity (v_{obs}) and v_{GK} was composited for 5 months of rain data to derive Equation 2. Each diameter class gets a dv shift according to the curve fit shown in Fig. 4, described by Eqn. 2. A condition is set to prevent the new velocity bin from surpassing the v_{GK} line.

Input for 'specshift':

- H_{xmin}
- t_x
- $v_{rawfall}$
- D

Output returned by 'specshift':

- $H_{shifted}$ = 'shiftspec,' shifted velocity-size histogram spectrum
  dimension: (t_x, $v_{rawfall}$, D); unit: counts
- w_{ratio}, mf_{ratio} - 'w_ratio, mf_ratio,' ratios of counts in wind and margin faller noise regions to total counts in spectrum
  dimension: t_x
- 'shift_track' = just there for me to track what algorithm did. Will be left out of finalized version.

C. metrics

This subroutine classifies the phase of precipitation by considering the populated bins in $H_{shifted}$. Equation 2 is used to calculate metrics m_T. The subscript T represents 'type' or phase of precipitation: wet snow (alternatively, mixed phase), ice pellets and snow.

$$m_T = \left(\sum_{i=1}^{32} \sum_{j=1}^{32} C_{i,j} \left[\frac{v_{\sigma_T}}{v_{\sigma_T} + \Delta v_T(i,j)} \right]^k \right) / \sum_{i=1}^{32} C_i \tag{3}$$

Subscripts i, j refer to the i^{th} diameter and j^{th} velocity bin; $C_{i,j}$ are the counts in one individual bin, C_i in the i^{th} diameter column; $\mathbf{v_{\sigma_T}}$ is the standard deviation of the spectrum used to calculate v_{fit} for each type; v_{fit} are the empirical fall speeds found by curve fitting various spectra (see section 3.1); $\mathbf{\Delta v_T(i,j)} = |v_{obs} - v_{fit}|$, the difference between an occupied velocity bin and v_{fit}; $k = 3$ was set by hand.

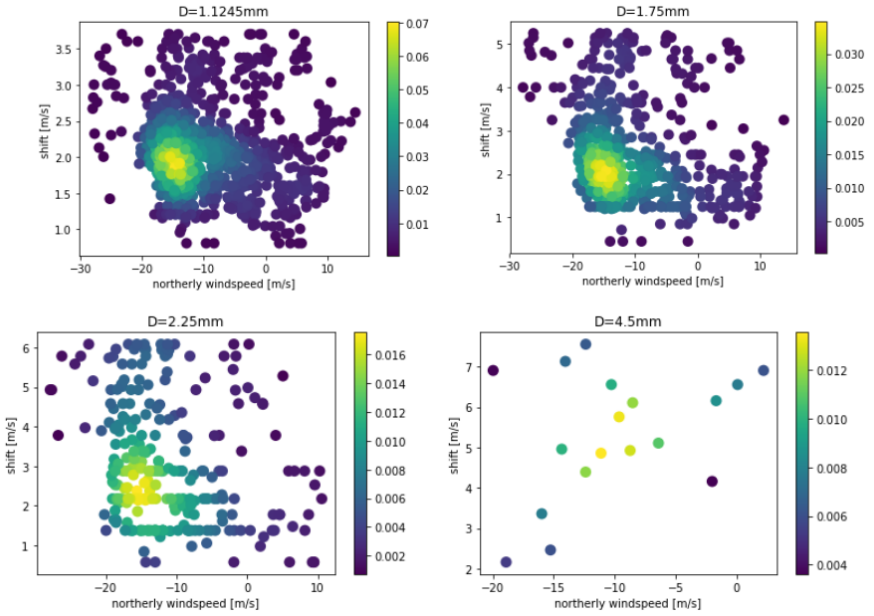

Figure 3: Necessary upward shift on velocity axis ($dv = v_{GK} - v_{obs}$) vs. northerly windspeed. The color bar shows normalized probability density. The scatterplot mean regions (yellow dots) occur at higher dv values as diameter increases. Uses MICRE data from April-August 2016 warm rain events.

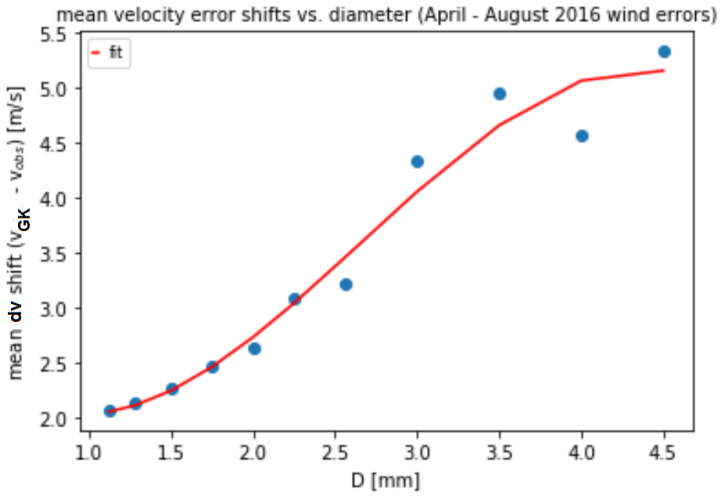

Figure 4: Polynomial curve fit for dv as a function of effective diameter. Blue points correspond to the probability density means (yellow centers) in Fig. 3. Uses MICRE data from April-August 2016 warm rain events.

C.1. Phase-specific fall speeds

As mentioned, the rain terminal fall speed equation is from literature. Empirical fall speeds for ice pellets and snow were calculated using the Parsivel vendor's designation of particle phase, called 'weather codes.'

Spectra from April-June 2016 were separated into snow and ice pellet histograms (according to the vendor's weather codes). After June 2016, a data loss deleted the rest of the weather codes. These two histograms were curve-fit to the form $v_{fit} = aD^b$, where

$$[a_{ip}, b_{ip}] = [2.476,\ 0.250] \text{ for ice pellets,}$$

$$[a_s, b_s] = [1.291,\ 0.353] \text{ for snow.}$$

The resulting v_{fit} for v_{ip} and v_{snow} were found to match up with fall speed equations from past studies. [Cornford, 1964; Magono & Nakamura, 1964; Locatelli & Hobbs, 1974]
The wet snow curve was derived by subtracting out rain, ice pellets, snow and noise regions (shown in Fig. 1) on the 2016 composited histogram. The remaining occupied bins are the 'wet snow' region between rain and frozen precipitation. This was curve-fit to $k_{ws} - a_{ws} * exp(-D^{b_{ws}})$, where $a_{ws} = -13.919$, $b_{ws} = -0.344$ and $k_{ws} = -1.783$ m/s.

C.2. $\mathbf{v}_{\sigma_t}$

The standard deviation of each diameter class was taken for the histograms used in the phase-specific fall speed calculations. $\mathbf{v}_{\sigma_t}$ are therefore four arrays with 32 elements for rain, ice pellets, snow and wet snow.

C.3. 'metrics' main algorithm

All counts in diameter bins < 1 mm are set to zero so only large particles, if present, impact the metrics. This is done because fall speeds in the small-particle regime differ only arbitrarily. m_T is calculated for each 5-minute spectrum.

C.3.1. 'Small' as a thermodynamic phase class

The < 1 mm mark defines the separation between large and small particles. If less than 5% of a histogram's counts are large and 1% or more of its total volume is attributed to small particles (without phase density correction), the spectrum's type is classified as 'small.'
Otherwise, the maximum m_T will determine the phase of a spectrum (with a few exceptions; Section 3.4). Assigned values are as follows:

- 0 = no weather
- 1 = rain
- 2 = ice pellets
- 3 = snow
- 4 = wet snow
- 5 = small

C.4. Secondary processing in 'metrics'

1) Spectra with m_r as the highest metric do not get classified as rain if there are 5 or more counts in diameter bins greater than 7 mm.
2) If subroutine 'specshift' failed to identify a spectrum in need of velocity shifting, or if the dv shift was not enough, rain spectra can get miscategorized as wet snow or ice pellets. A secondary process in 'metrics' looks at all type classifications in the 30 minutes surrounding a timestep.

- If a classification is the only wet snow/ice pellet class in that 30 minutes, surrounded by rain and small classes, and $m_{wetsnow} - m_{rain} < 0.15$, the class is changed from wet snow/ice pellet to rain.

3) Instrument calibration is also flagged in the secondary processing. The instrument calibrates by pulsing the laserbeam. This outputs a histogram of many randomly distributed counts detected over 1-2 minutes. This is flagged and denoted in the data quality output.

Input for 'metrics':

- t_x
- $v_{rawfall}$, D
- H_{shift}, H_{xmin}
- w_{ratios}, mf_{ratios}
- DQ

Output returned by 'metrics':

- m_T = metrics for rain, wet snow, ice pellets and snow

  dimension: t_x

- $m_{1mm}^{constant}$ = metric that indicates ≥95% of counts are in small bins (0='no,' 1='yes');

  m_{1mm}^{vols} = ratio of volume in small bins to overall volume

  dimension: t_x

- P_{PIRAT} = 'my_wcs,' phase classifications of H_{shift}

  dimension: t_x

- c_{ws} designator = 'cws_designator,' designates which density correction should be used for wet snow classes in 'rates_calculation' subroutine.

  1) Compare —m_ip - m_{ws}— and —m_r - m_{ws}—.

  2) If m_{ws} is more similar to m_{ip}, use a less dense coefficient in rates calculation. If m_{ws} is more similar to m_r, use a denser coefficient.

  dimension: t_x

- DQ

D. rates_calculation

This subroutine calculates and outputs the precipitation rate for each phase of precipitation, regardless of class assigned by 'metrics.' It also returns the main rates vector containing phase-specific values. Some filtering is done based on statistics of that day's precipitation in order to decrease unrealistically high values. Effective radius and particle size distribution (PSD) corresponding to each H_{shift} are also calculated, as well as a daily PSD.

D.1. Renormalization

The spectrum is renormalized only if the class is 'small,' i.e. $P_{PIRAT} = 5$. A spectrum is renormalized if

- mf_{ratio} or $w_{ratio} \geq 0.5$ (i.e., there is a lot of noise)
- non-noise spectral sum $\sum_{\mathbf{i=1}}^{\mathbf{32}} \sum_{\mathbf{j=1}}^{\mathbf{32}} H_{shift}^{i,j} \geq$ 30% of counts in the noise regions

Renormalization is done by adding 50% of neglected noise counts to each ith diameter column's median *velocity* bin, considering only populated diameter columns.

D.2. Number concentration and PSD

The laserbeam sampling cross section is defined by length $L = 0.180$ m and width $B = 0.03$ m. The Parsivel sampling area is then

$$S = L \cdot (B - \frac{\bar{D}_i \cdot 10^{-3}}{2}) \tag{4}$$

where $\bar{D}_i$ [unit: mm] is the midpoint of the ith diameter class. Concentration of drops are calculated using this sampling area. [Jaffrain & Berne, 2010] For the ith diameter of a 5-minute spectrum, the number concentration N_i is

$$N_i = \frac{1}{S \cdot dD_i \cdot dt} \cdot \sum_{j=1}^{32} \frac{C_j}{\bar{v}_{fall}^j} \tag{5}$$

where dD_i [unit: mm] is the spacing of the ith diameter class. C_j are counts in the jth velocity bin and $\bar{v}_{fall}^j$ [unit: m/s] is its midpoint. Sampling time is $dt = d_x \cdot 60$ seconds, in this case, 300 seconds.
A daily PSD is constructed by averaging each diameter class over all spectra.

D.3. Hydrometeor effective radius

The effective radius for the xth spectrum of the day (r_{eff}^x) is found using the PSD third moment divided by the second moment.

$$r_{eff}^x = \frac{1}{2} \cdot \frac{\sum_{i=1}^{32} N_i \cdot D_i^3 \cdot dD_i}{\sum_{i=1}^{32} N_i \cdot D_i^2 \cdot dD_i} \tag{6}$$

D.4. Precipitation rates

The general rate equation used for precipitation of phase type T is

$$R_T(D) = c_T \cdot 6\pi \cdot 10^{-4} \int_{D_{i=1}}^{D_{i=32}} N_i \cdot v_T^{fit}(D_i) \cdot D_i^3 \tag{7}$$

in [mm/hour]. The density correction coefficient c_T simplifies to 1 for rain and drizzle ($\rho_{\mathbf{liquid}} = 0.997$ g·cm^{-3}), whereas it decreases $R_T(D)$ for frozen and semi-frozen precipitation. The following density corrections are used:

$$c_{ip} = \frac{\rho_{\mathbf{liquid}} - \rho_{\mathbf{ice}}}{\rho_{\mathbf{liquid}}} \text{ where } \rho_{ice} = 0.934 \text{ g·cm}^{-3} \text{ (ice pellets)}$$

$$c_s(D) = \frac{\rho_{\mathbf{snow}}}{\rho_{\mathbf{liquid}} + \rho_{\mathbf{snow}}} \text{ where } \rho_{snow} = 0.178 \cdot D^{-0.922} \text{ in g·cm}^{-3} \text{ (snow)}$$

$$c_{ws}(D) = \left(\frac{\mathbf{v_{wetsnow}^{fit}}}{\mathbf{v_{snow}^{fit}}}\right)^{\mathbf{g}} \cdot c_s(D) \text{ (wet snow)}$$

where $g = 2$ when mostly melted, $g = -1/3$ when mostly frozen, as specified by the c_{ws} designator from 'metrics'.

The general forms of each coefficient were set to decrease $R_T(D)$ an amount comparable to rates reflected by the tipping bucket and, in the case of c_s, to align with past studies. [Magono & Nakamura, 1964] Densities for various frozen precipitation classes are from Locatelli & Hobbs, 1974.

D.5. Secondary processing: switching the phase of 'small' timesteps

The rate at each timestep is calculated for each phase of precipitation, regardless of P_{PIRAT}. Secondary processing was added after noting that, in several periods of small-particle precipitation, PIRAT produced rates that were too high. These intervals were surrounded by wet snow, ice pellets and/or snow events.
To address this, a 20 minute window checks whether any rain is present. If large-particle precipitation is all frozen ±10 minutes around the 'small' spectra, the rate retrieval is changed to reflect the appropriate phase.

D.6. Secondary processing: filtering out unrealistic values

Anomalously high rates are filtered using statistics of that day's precipitation distribution. Unrealistic values are set to the daily median for that hydrometeor type under the following conditions:

- $R > 20$ mm/hour, or $R > R_{med}^{rain} + 4$ standard deviations (P_{PIRAT} = rain)
- $R > 8$ mm/hour, or $R > R_{med}^{small} + 4$ standard deviations (P_{PIRAT} = small)
- $R > R_{med}^{ip} + 4$ standard deviations (P_{PIRAT} = ice pellets)
- $R > R_{med}^{ws} + 4$ standard deviations or $R > 50 \cdot R_{med}^{ws}$ (P_{PIRAT} = wet snow)

  (A factor of 50 is used in lieu of standard deviation because wet snow rates and spectra tend to have higher variance.)
- $R > 7$ mm/hour or $R > R_{med}^{s} + 4$ standard deviations (P_{PIRAT} = snow)

Input for 'rates_calculation':

- t_x, d_x
- $v_{rawfall}$, D
- H_{shift}, H_{xmin}
- c_{ws} designator
- P_{PIRAT}

Output returned by 'rates_calculation':

- R = precipitation rate array. Elements are specific to weather type identified in P_{PIRAT}.

  dimension: t_x; unit: mm/hour

- $R_{rain}, R_{ip}, R_{snow}, R_{ws}$ = precipitation rate arrays as if all weather were rain, ice pellets, snow and wet snow, respectively.

  dimension: t_x; unit: mm/hour

- R_{drz} = array of rates using small-particle bins only, even in cases where large particles were present. Cutoff bin for a spectrum's drizzle/small-particle counts is D=1 mm.

  dimension: t_x; unit: mm/hour

- N_{t_x} = 'N_n_tx,' particle size distributions for each 5-min spectrum

  dimension: (t_x, D); unit: $m^{-3}mm^{-1}$

- N_{dayavg} = particle size distribution for all precipitation that day

  dimension: D; unit: $m^{-3}mm^{-1}$

- r_{eff} = 'r_eff_tx,' array of effective radii for each 5-min spectrum

  dimension: t_x; unit: mm

E. scale_spectra

'Scale_spectra' increases counts in H_{shift}. H_{shift} is scaled by α, a function of *(i)* hydrometeor phase and *(ii)* median A_{laser} across 5 minutes (or whatever resolution is chosen for H_{shift}). The scaling is linear, following the simple relation

$$H_{shift}^{scaled} = \alpha(A_{laser}, P_{PIRAT}) \cdot H_{shift} \tag{8}$$

This subroutine was developed in response to observed underaccumulation of liquid equivalent volume. Comparing both the Parsivel vendor's retrieval and PIRAT to the tipping bucket indicates that the instrument's raw detections come up short far more often than not.
The Parsivel is considered non-operating when $A_{laser} < 5000$, in need of immediate maintenance when $A_{laser} < 7500$ and in need of eventual maintenance when $A_{laser} < 10,000$. These conditions are characteristic of 22%, 20% and 27% of the MICRE dataset, respectively. Spectra should be scaled as needed to process as many measurements as possible and derive microphysical parameters.

E.1. Spectral scaling factor $\alpha(A_{laser}, P_{PIRAT})$

Difference minimization between PIRAT's cumulative volume and the tipping bucket accumulation was composited for 4 months (April-July 2016). These months contained a variety of light, heavy and mixed precipitation events at a variety of laser-band amplitudes.
The tipping bucket tips after 0.2 mm of accumulation. The 5-min velocity-size histogram H_{shift} is scaled by α values going from 1 to 51 in steps of 1. 51 was chosen arbitrarily as the maximum scaling factor. H_{shift}^{scaled} is then fed into 'rates_calculation.' H_{shift}^{scaled} yields a higher rate. The new PIRAT accumulation at that timestep is compared to the tipping bucket again. α is increased until the PIRAT accumulation is $\leq$ TB - 0.2 mm (simple schematic in Fig. 5).

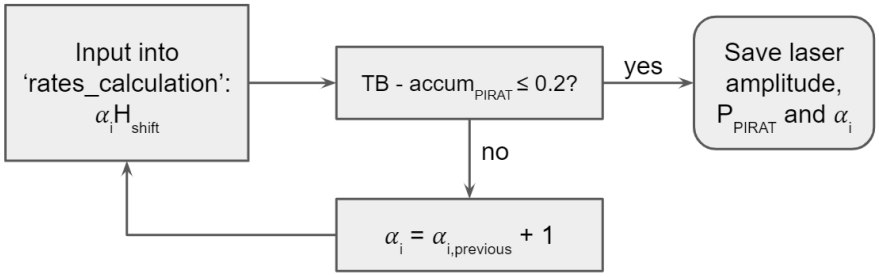

Figure 5: Difference minimization between tipping bucket and PIRAT accumulation $accum_{PIRAT}$ as scaling factor α is increased from 1 to 50 in steps of 0.5.

E.2. k-means clustering of α vs. A_{laser} by hydrometeor class

The difference minimization described above stores three variables: *(i)* α_i, *(ii)* median A_{laser} over that 5 minutes and *(iii)* P_{PIRAT}. This is scaled down to 2 dimensions by sectioning off (α, A_{laser}) points into different precipitation phases.
k-means clustering is performed on (α, A_{laser}) scatterplots for $P_{PIRAT} = 1$ through 5. k is chosen to be 5. The tables on the next page show the mean α and A_{laser} of each cluster.

E.3. Further conditions imposed in 'scale_spectra'

E.3.1. High-sum spectra

Overaccumulation happens when a spectrum yields unrealistically high precipitation rates over a brief period of time in comparison to the tipping bucket. Although Parsivel undercounting is more common than overcounting, the latter occurs on occasion too. Overcounting is a potential source of overaccumulation. Spectra shouldn't be scaled in this case, as it exacerbates unreal spikes in accumulated precipitation.
Spectral count statistics were calculated for phase-separated spectra from the first year of MICRE data. As a value for comparison, the median number of counts in a phase-specific 5-minute spectrum was chosen. Median instead of mean is used since counts are gamma-distributed (Fig. 6).

E.3.2. Ambiguous phase spectra

Overaccumulation can also result from misidentifying large frozen particles as raindrops, thereby failing to correct their density in 'rates_calculation.' This is obviously harder to identify; errors made in an earlier subroutine cannot be identified unless ancillary data is used. When ancillary data is used, PIRAT lacks objectivity. Conditions **4)** and **5)** below attempt to identify spectra with phase ambiguity.

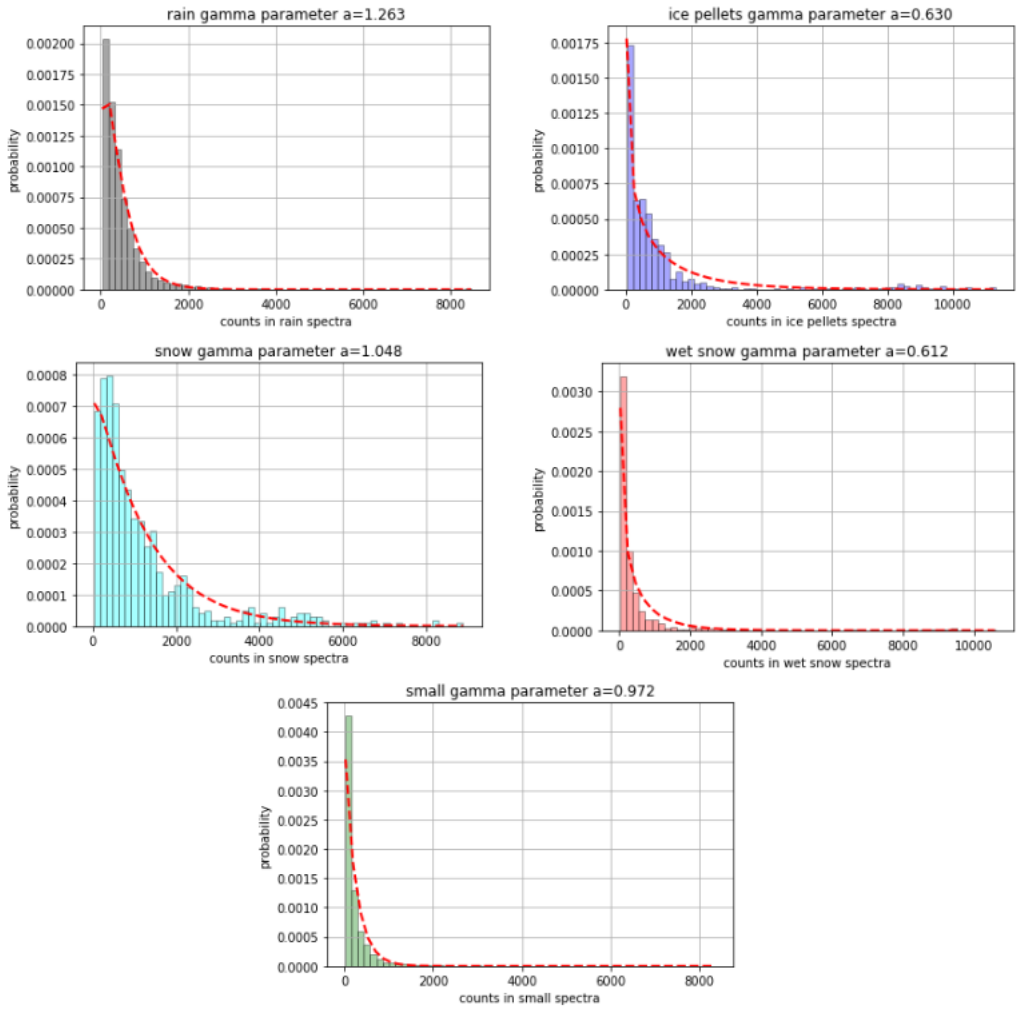

Figure 6: Gamma-distributed size-velocity histogram total counts from April 2016 - March 2017, separated by phase.

Five conditions to prevent α-scaling when it might cause overaccumulation:
1) Spectra with total counts greater than three standard deviations from the median (predetermined for each phase; see Fig. 6).
2) For $A_{laser} > 10{,}000$, spectra with total counts greater than two standard deviations.
3) For P_{PIRAT} = 'small,' spectra that have already been renormalized using noise counts (described in Section 4.1).
4) A 30 minute window of P_{PIRAT} surrounds the timestep of interest. *(i)* If $w_{ratio} > 0.05$ and *(ii)* the 30 minute window contains 2 or more ice pellet or wet snow classifications, the spectrum of interest is considered uncertain.
5) *(i)* If there are 3 or more ice pellet, wet snow or snow classifications that day and *(ii)* the spectrum's standard deviation is more than 1.5x the standard deviation of the whole day spectrum.

Input for 'scale_spectra':

- H_{shift}
- P_{PIRAT}

- $A_{laser}^{missing}$
- d_x
- w_{ratios}
- DQ

Output returned by 'scale_spectra':

- H_{shift}^{scaled} = the output of 'shiftspec' scaled by $\alpha(A_{laser}, P_{PIRAT})$
  dimension: $(t_x, v_{rawfall}, D)$; unit: counts

Phase-specific α and laserband amplitude ranges from k-clusters

P_{PIRAT} = small	
A_{laser} range	α
0 - 6233	8.304
6233 - 8596	7.62
8596 - 10,870	9.135
10,870 - 13,151	11.016
13,151 - 16,139	3.171

P_{PIRAT} = rain	
A_{laser} range	α
0 - 5508	3.387
5508 - 8246	5.113
8246 - 10,332	2.141
10,332 - 12,143	2.23
12,143 - 15,921	1.0

P_{PIRAT} = wet snow	
A_{laser} range	α
0 - 5650	1.209
5650 - 8381	1.721
8381 - 10,487	1.9
10,487 - 12,804	2.765
12,804-16,190	0.5

P_{PIRAT} = ice pellets	
A_{laser} range	α
0 - 5550	2.674
5550 - 7910	4.274
7910 - 9765	1.483
9765 - 11,675	6.936
11,675 - 15,904	5.0

P_{PIRAT} = snow	
A_{laser} range	α
0 - 4966	1.0
4966 - 7395	1.857
7395 - 9320	1.147
9320 - 11, 734	2.494
11734 - 14,138	1.0